

This work was written as part of one of the author's official duties as an Employee of the United States Government and is therefore a work of the United States Government. In accordance with 17 U.S.C. 105, no copyright protection is available for such works under U.S. Law.

CC0 1.0 Universal (CC0 1.0)

Public Domain Dedication

<https://creativecommons.org/publicdomain/zero/1.0/>

Access to this work was provided by the University of Maryland, Baltimore County (UMBC) ScholarWorks@UMBC digital repository on the Maryland Shared Open Access (MD-SOAR) platform.








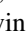




**Please provide feedback**

Please support the ScholarWorks@UMBC repository by emailing [scholarworks-group@umbc.edu](mailto:scholarworks-group@umbc.edu) and telling us what having access to this work means to you and why it's important to you. Thank you.



# The EBEX Balloon-borne Experiment—Optics, Receiver, and Polarimetry

The EBEX Collaboration,

Asad M. Aboobaker<sup>1,2,20</sup>, Peter Ade<sup>3</sup> , Derek Araujo<sup>4</sup> , François Aubin<sup>1,5,20</sup> , Carlo Baccigalupi<sup>6,7</sup>, Chaoyun Bao<sup>1</sup>, Daniel Chapman<sup>4</sup>, Joy Didier<sup>4,8,20</sup> , Matt Dobbs<sup>5,9</sup>, Christopher Geach<sup>1</sup>, Will Grainger<sup>10</sup>, Shaul Hanany<sup>1</sup> , Kyle Helson<sup>11,12,20</sup> , Seth Hillbrand<sup>4</sup>, Johannes Hubmayr<sup>13</sup>, Andrew Jaffe<sup>14</sup> , Bradley Johnson<sup>4</sup>, Terry Jones<sup>1</sup>, Jeff Klein<sup>1</sup>, Andrei Korotkov<sup>11</sup>, Adrian Lee<sup>15</sup>, Lorne Levinson<sup>16</sup> , Michele Limon<sup>4</sup> , Kevin MacDermid<sup>5</sup>, Tomotake Matsumura<sup>1,17,20</sup>, Amber D. Miller<sup>4,8,20</sup>, Michael Milligan<sup>1</sup>, Kate Raach<sup>1</sup>, Britt Reichborn-Kjennerud<sup>4</sup>, Ilan Sagiv<sup>16</sup> , Giorgio Savini<sup>18</sup>, Locke Spencer<sup>3,19,20</sup>, Carole Tucker<sup>3</sup>, Gregory S. Tucker<sup>11</sup> , Benjamin Westbrook<sup>15</sup>, Karl Young<sup>1</sup> , and Kyle Zilic<sup>1</sup> 

<sup>1</sup> University of Minnesota School of Physics and Astronomy, Minneapolis, MN 55455, USA; [hanany@umn.edu](mailto:hanany@umn.edu)

<sup>2</sup> Jet Propulsion Laboratory, California Institute of Technology, Pasadena, CA 91109, USA

<sup>3</sup> School of Physics and Astronomy, Cardiff University, Cardiff, CF24 3AA, UK

<sup>4</sup> Physics Department, Columbia University, New York, NY 10027, USA

<sup>5</sup> Department of Physics, McGill University, Montreal, Quebec, H3A 2T8, Canada

<sup>6</sup> Astrophysics Sector, SISSA, Trieste, I-34014, Italy

<sup>7</sup> INFN, Sezione di Trieste, Via Valerio 2, I-34127 Trieste, Italy

<sup>8</sup> Department of Physics and Astronomy, University of Southern California, Los Angeles, CA 90089, USA

<sup>9</sup> Canadian Institute for Advanced Research, Toronto, ON M5G1Z8, Canada

<sup>10</sup> Rutherford Appleton Lab, Harwell Oxford, OX11 0QX, UK

<sup>11</sup> Brown University, Providence, RI 02912, USA

<sup>12</sup> NASA Goddard Space Flight Center, Greenbelt, MD 20771, USA

<sup>13</sup> National Institute of Standards and Technology, Boulder, CO 80305, USA

<sup>14</sup> Department of Physics, Imperial College, London, SW7 2AZ, UK

<sup>15</sup> Department of Physics, University of California, Berkeley, Berkeley, CA 94720, USA

<sup>16</sup> Faculty of Physics, Weizmann Institute of Science, Rehovot 76100, Israel

<sup>17</sup> Kavli Institute for the Physics and Mathematics of the Universe (Kavli IPMU, WPI), Todai Institutes for Advanced Study, The University of Tokyo, Kashiwa City, Chiba 277-8583, Japan

<sup>18</sup> University College London, London WC1E 6BT, UK

<sup>19</sup> University of Lethbridge, Lethbridge, AB, T1K 3M4, Canada

Received 2017 May 28; revised 2017 November 17; accepted 2017 November 22; published 2018 November 6

## Abstract

The E and B Experiment (EBEX) was a long-duration balloon-borne cosmic microwave background (CMB) polarimeter that flew over Antarctica in 2012. We describe the experiment’s optical system, receiver, and polarimetric approach and report on their in-flight performance. EBEX had three frequency bands centered on 150, 250, and 410 GHz. To make efficient use of limited mass and space, we designed a 115 cm<sup>2</sup> sr high-throughput optical system that had two ambient temperature mirrors and four antireflection-coated polyethylene lenses per focal plane. All frequency bands shared the same optical train. Polarimetry was achieved with a continuously rotating achromatic half-wave plate (AHWP) that was levitated with a superconducting magnetic bearing (SMB). This is the first use of an SMB in astrophysics. Rotation stability was 0.45% over a period of 10 hr, and angular position accuracy was 0°.01. The measured modulation efficiency was above 90% for all bands. To our knowledge the 109% fractional bandwidth of the AHWP was the broadest implemented to date. The receiver, composed of one lens and the AHWP at a temperature of 4 K, the polarizing grid and other lenses at 1 K, and the two focal planes at 0.25 K, performed according to specifications, giving focal plane temperature stability with a fluctuation power spectrum that had a 1/*f* knee at 2 mHz. EBEX was the first balloon-borne instrument to implement technologies characteristic of modern CMB polarimeters, including high-throughput optical systems, and large arrays of transition edge sensor bolometric detectors with multiplexed readouts.

*Key words:* balloons – cosmic background radiation – cosmology: observations – instrumentation: polarimeters – polarization

## 1. Introduction

Measurements of the cosmic microwave background (CMB) have provided a wealth of information about the physical mechanisms responsible for the evolution of the universe. In recent years, experimental efforts have focused on measuring the CMB’s polarization patterns: *E*-modes and *B*-modes (Zaldarriaga & Seljak 1997). The level and specific shape of the angular power spectrum of CMB *E*-mode polarization can

be predicted given the measured intensity anisotropy. Lensing of *E*-modes by the large-scale structure of the universe produces cosmological *B*-modes at small angular scales, while an inflationary phase at sufficiently high energy scales near the big bang is predicted to leave another detectable *B*-mode signature at large and intermediate angular scales (Baumann et al. 2009).

The *E*-mode polarization of the CMB was first detected by the DASI experiment (Kovac et al. 2002), and other experiments soon followed suit (Scott & Smoot 2010). The combination of all measurements is in excellent agreement

<sup>20</sup> Current affiliation.

with predictions.  $B$ -mode polarization from gravitational lensing of  $E$ -modes and from Galactic dust emission has also recently been detected (Hanson et al. 2013; Ade et al. 2014; BICEP2 Collaboration et al. 2014; Naess et al. 2014; BICEP2/Keck and Planck Collaborations et al. 2015). Intense efforts are ongoing by ground- and balloon-based instruments to improve the measurements, separate the Galactic from the cosmological signals, and identify the inflationary  $B$ -mode signature.

The E and B Experiment (EBEX) was a balloon-borne CMB polarimeter striving to detect or constrain the levels of the inflationary gravitational wave and lensing  $B$ -mode power spectra. EBEX was also designed to be a technology pathfinder for future CMB space missions. To improve instrument sensitivity, we implemented a kilopixel array of transition edge sensor (TES) bolometers and planned for a long-duration balloon flight. We included three spectral bands centered on 150, 250, and 410 GHz to give sensitivity to both the CMB and the galactic dust foreground. The combination of the 400 deg<sup>2</sup> intended survey size and an optical system with 0.1 resolution gave sensitivity to the range  $30 < \ell < 1500$  of the angular power spectrum. Polarimetry was achieved with a continuously rotating achromatic half-wave plate (HWP).

Several new technologies have been implemented and tested for the first time in the EBEX instrument. It was the first balloon-borne experiment to implement a kilopixel array of TES bolometric detectors. It was also the first to implement a digital frequency domain multiplexing system to read out the TES arrays; this digital system was later adopted by a number of ground-based experiments. Finally, it was the first astrophysical instrument to implement and operate a superconducting magnetic bearing (SMB), which was used to levitate the HWP.

Design and construction of the experiment began in 2005. A 10 hr engineering flight was launched from Ft. Sumner, NM, on 2009 June 11, and the long-duration science flight was launched from McMurdo Station, Antarctica, on 2012 December 29. Because the majority of the 25-day long-duration flight was in 2013 January, we refer to this flight as EBEX2013.

This paper is one of a series of papers describing the experiment and its in-flight performance. This paper, called EBEX Paper 1, discusses the telescope and the polarimetric receiver, EBEX Paper 2 (EP2; The EBEX Collaboration 2018a) describes the detectors and the readout system, and EBEX Paper 3 (EP3; The EBEX Collaboration et al. 2018b), describes the gondola, the attitude control system, and other support systems. Several other publications give additional details about the EBEX experiment. Some are from earlier stages of the program (Oxley et al. 2004; Grainger et al. 2008; Aubin et al. 2010; Milligan et al. 2010; Reichborn-Kjennerud et al. 2010; Klein et al. 2011; Sagiv et al. 2012; Westbrook et al. 2012), and others discuss some subsystems in more detail (Polsgrove 2009; Reichborn-Kjennerud 2010; Sagiv 2011; Aubin 2012; MacDermid 2014; MacDermid et al. 2014; Westbrook 2014; Zilic 2014; Chapman 2015; Chapman et al. 2015; Didier et al. 2015; Aubin et al. 2016; Didier 2016).

The science goals of EBEX and the choice of technical implementation placed constraints on the design and operation of the instrument. In Section 2 we describe the EBEX optical system, including the warm telescope, the cold optics, and the frequency bands. The optical system was designed to

provide a resolution of 5–10', sufficient to probe the lensing signal at  $\ell \simeq 1000$ . It also gave a flat and telecentric focal surface to accommodate the array of TESs that were fabricated on silicon arrays. This optical system required lenses to enhance the throughput provided by the two warm mirrors. The lenses, the focal planes, and the cryogenic refrigerators that kept them at temperatures below ambient are described in Section 3. We implemented an achromatic half-wave plate (AHWP) because it made efficient use of the throughput for the three frequency bands. We used it in continuous rotation to avoid low-frequency noise. In Section 4 we discuss the implementation of the AHWP, the SMB, the rotation mechanism, and the polarimetric calibration.

## 2. Telescope and Optics

### 2.1. Optical Design

The EBEX optical system consisted of an off-axis Gregorian reflecting telescope coupled to a cryogenic receiver containing refractive optics, a rotating AHWP at a cold aperture stop, and a polarizing grid that directed independent polarizations to each of two focal planes; see Figure 1.

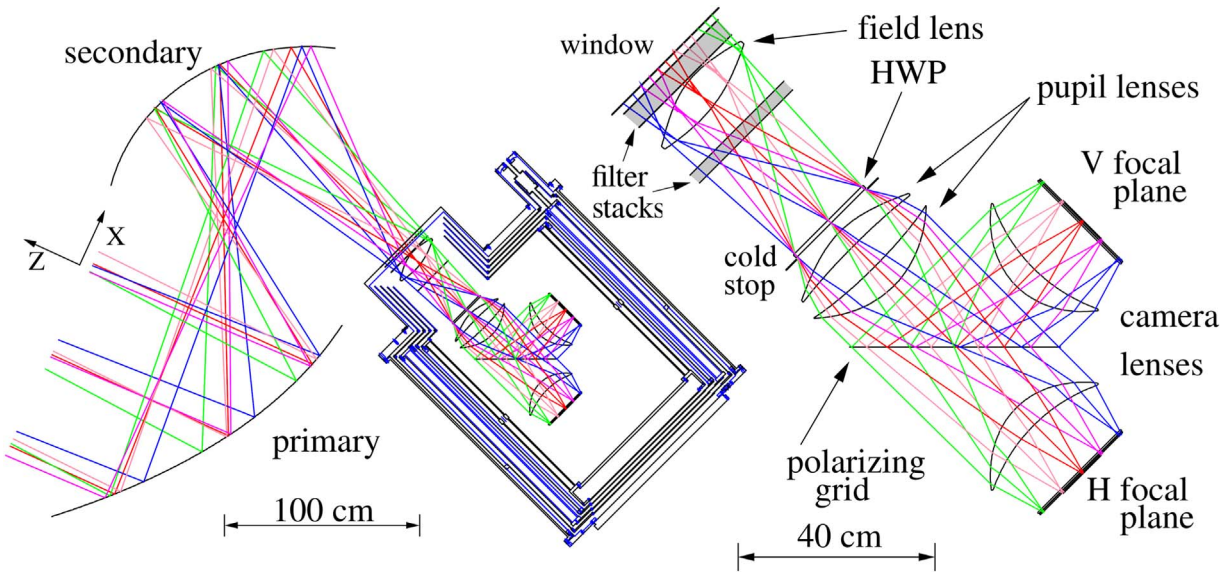
The parabolic off-axis primary mirror collected incoming radiation and, via an elliptical secondary, formed the Gregorian focal surface 10 cm behind the vacuum window of the receiver. A field lens was placed coincident with this focal surface and was tilted 8.1° from the optical axis. The field lens formed an image of the primary at the cold aperture stop, which was immediately after the AHWP. Past the cold stop a pair of pupil lenses collimated the ray bundle. A wire grid linear polarizer passed one state of polarization and reflected another, forming two optical branches. Camera lenses on each branch formed the final flat, telecentric focal planes, denoted as H (horizontal) and V (vertical) for the branches that were transmitted and reflected by the grid, respectively. At the focal plane conical feeds backed by circular waveguides coupled the light from free space into the detector cavities. The reflectors and cryostat were mounted on the gondola's inner frame and were surrounded by baffles to control sidelobe pickup.

### 2.2. Ambient Temperature Telescope

The ambient temperature telescope was an off-axis Gregorian Mizuguchi–Dragone design (Mizuguchi et al. 1978; Dragone 1982) with an entrance aperture of 1.05 m, defined by the cold stop. The  $f$ -number varied across the field of view (FOV) by up to 10%, with an average of  $f/1.9$ . The telescope geometry is shown in Figure 2, and the parameters of the design are tabulated in Table 1. To minimize sidelobe pickup due to spillover power, both the primary and secondary mirrors were 1.4 times larger than the size defined by ray-tracing of a 1.05 m entrance aperture diameter. All ray-tracing analysis used a 1.05 m aperture apodized by the Gaussian illumination from the feed horns as appropriate for each frequency band; see Section 2.3.

The 1.5 × 1.8 m parabolic primary mirror weighed 42 kg and was previously used in Archeops (Benoît et al. 2002). The 1.2 × 1.3 m and 22 kg secondary, a section of an ellipsoid of revolution, was fabricated for EBEX.<sup>21</sup> Each mirror was machined from a single billet of 6061-aluminum. The mirrors

<sup>21</sup> Machining by Remmele Engineering, New Brighton, Minnesota.



**Figure 1.** Ray-tracing of the EBEX optical design consisting of two ambient temperature reflectors in a Gregorian configuration and a cryogenic receiver (left). Inside the receiver (right), cryogenically cooled polyethylene lenses formed a cold stop and provided diffraction-limited performance over a flat, telecentric,  $6^\circ 6'$  FOV. A continuously rotating achromatic half-wave plate placed near the aperture stop and a polarizing grid provided the polarimetry capabilities.

had a 5 mm thick reflecting surface backed by a hexagonal rib structure designed to provide stiffness during surface machining while minimizing weight. The rough machined mirrors were heat treated to the T6 condition before the last  $250\ \mu\text{m}$  were milled from the reflecting surface. The machined mirror surfaces had roughness of less than  $2\ \mu\text{m}$ . Additionally, small areas at the center and at the  $\pm x$  and  $\pm y$  edges of each reflector were polished to optical quality to enable laser alignment. We measured the primary and secondary mirror surface contours using a tooling ball laser probe and found rms figure accuracies of 51 and  $48\ \mu\text{m}$ , respectively. This figure accuracy was 1/13 of the wavelength at the highest edge of the highest-frequency band.

### 2.3. Receiver Cold Optics and Focal Planes

The receiver cold optics formed a reimaging camera that transferred the image formed at the Gregorian focus to the focal planes. The  $f$ -number was approximately preserved, while the camera hosted an internal aperture stop, enlarged the diffraction-limited FOV, and formed two flat, telecentric focal planes. The receiver section of the light path also included electromagnetic filters, the AHWP, and a polarizing wire grid beam splitter.

Optical elements inside the receiver were heat sunk to several distinct temperature stages. The vacuum window was at ambient temperature; the field lens and the AHWP were at liquid helium temperature; the aperture stop, pupil lenses, and camera lenses were at approximately 1 K; and the focal planes operated near 0.25 K.

To ensure consistent material properties, we machined all the lenses from a single block of ultrahigh molecular weight polyethylene (PE). We measured a sample of this PE at room temperature in a Fourier transform spectrometer and found the index of refraction to be  $n = 1.503 \pm 0.002$  with no detectable birefringence ( $\delta n < 0.004$ ). Extrapolation to 4 K using the Lorentz–Lorenz equation with linear contraction between 1.5 and 2% gives a predicted cold index between 1.53 and 1.54.

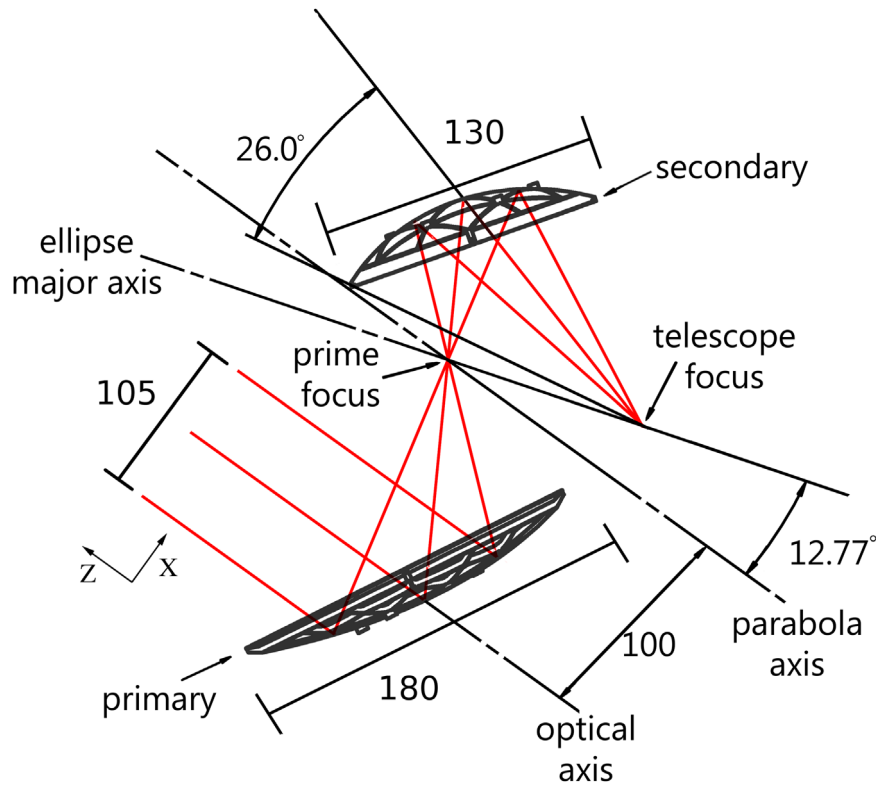
We optimized the lens shapes using the ray-tracing codes CodeV<sup>22</sup> and ZEMAX.<sup>23</sup> The optimization constrained solutions to a flat and telecentric focal plane while maximizing the diffraction-limited FOV so as to accommodate as large a number of detectors as possible. Due to an error, we used  $n = 1.52$  in the optimization. We discuss the consequences of this error in Section 2.7. All designed lens surfaces were conic sections of revolution. With  $n = 1.52$  the designed lenses provided a diffraction-limited FOV with Strehl ratio above 0.8 across the entire focal plane, as shown in Figure 3. The total throughput of the optical system for each focal plane was  $115\ \text{cm}^2\ \text{sr}$ .

Each of the two EBEX focal planes consisted of a layer of band-defining electromagnetic filters, a monolithic array of feed horns attached to a monolithic array of waveguides, seven detector wafers, wafer holders and “inductor and capacitor (LC) Boards,” and a back cover that, together with the array of waveguides, completed a Faraday cage around the detectors; see Figure 4. The electromagnetic filters and waveguides defined three frequency bands centered on 150, 250, and 410 GHz. The focal plane was arranged such that four wafers operated at 150 GHz, two at 250 GHz, and one at 410 GHz. The LC boards were part of the multiplexed frequency domain bias and readout of the detectors, which are discussed in more detail in EP2. Each detector wafer had 128 wired detectors that were biased and read out with eight pairs of wires.

The arrays of smooth-walled feed horns coupled the radiation from free space to an array of waveguides with chokes; see Figure 4. The horns were truncated cones with an entrance diameter of 6.37 mm and a length of 23 mm for all frequency bands. The exit diameter was 1.32, 0.81, and 0.48 mm for the 150, 250, and 410 GHz bands, respectively, matching the waveguide diameters immediately below the feed horns. The waveguide plate was 10 mm thick. We spaced the horns and detectors at  $1.74\ f\lambda$  for 150 GHz, which was

<sup>22</sup> Synopsys Optical Solutions.

<sup>23</sup> OpticStudio from ZEMAX.



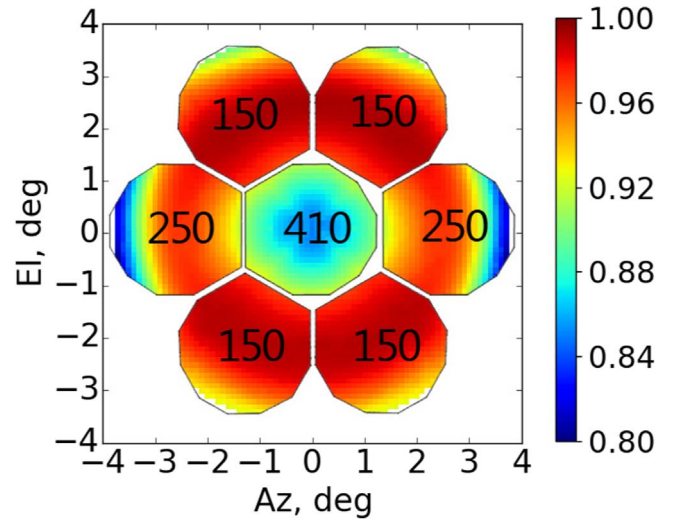
**Figure 2.** Geometry of the EBEX Gregorian-Dragone reflecting telescope. Lengths are in cm.

**Table 1**  
Gregorian Telescope Parameters

Effective focal length	198 cm
Aperture diameter	105 cm
PR focal length	80 cm
$\angle$ between PR and SR axes	12°77
PR offset	100 cm
SR semimajor axis length, $a$	110.2 cm
SR semiminor axis length, $b$	98.21 cm
SR conic constant, $K$	-0.2059
SR opening half-angle	26°
PR maximum size	1.5 × 1.8 m
SR maximum size	1.2 × 1.3 m

**Note.** Five fundamental parameters define the geometry of an off-axis Gregorian Telescope (upper section). PR (SR) denotes the primary (secondary) reflector. The middle section lists derived parameters relevant to telescope fabrication. The physical mirror dimensions (lower section) are the full fabricated size of the mirrors and are 1.4 times larger than the ray-tracing apertures.

6.626 mm. The horn length maximized the 410 GHz band gain with a moderate reduction in the gain of the other two bands (King 1950). The predicted gain at 150 and 250 GHz was 84% and 93% of the maximum, respectively. We machined the feed horn array and waveguide array each from a single piece of aluminum. Before machining, they were aligned with dowel pins and bolted together. The horns were machined with a custom cutter that marked the waveguide centers. Then the horn array was removed, the waveguides were drilled, and both pieces were plated with a 0.127  $\mu\text{m}$  gold layer. The horn array was then reattached to the waveguides using the dowel pins to ensure alignment. We optimized the

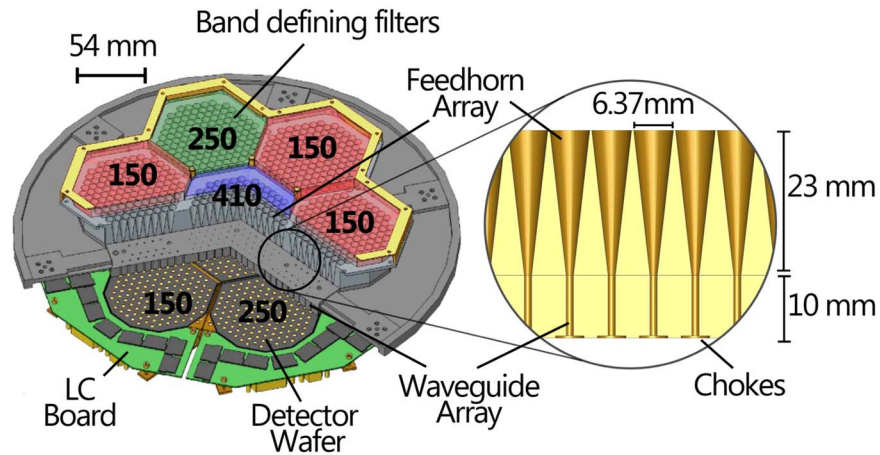


**Figure 3.** Detector wafer outlines on the focal plane, overlaid by Strehl ratios, with frequency denoted as a number at the center of each wafer. We improved optical performance near the edge of the field of view at the expense of performance at the focal plane center. Strehl ratios are not shown beyond 3°8 in radius, as these fields are strongly vignetted, causing ray-tracing codes to fail.

optics for the 150 GHz band by aligning the 150 GHz feed horns to the focus of the telescope optics. This defocused the 250 and 410 GHz feed horns. The predicted loss in coupling efficiency at 410 GHz, where the defocusing was the largest, was only 3%.

#### 2.4. Telescope Alignment

The focal planes were the reference for the alignment of the entire optical system. They had no adjustable degrees of



**Figure 4.** EBEX focal plane (left). The observing bands are defined by filters and waveguides (see Section 2.6). Conical feed horns coupled the detectors to free space; see Section 2.3. Seven wafers held 141 bolometers each at 150, 250, or 410 GHz. Below the wafers were LC boards, the first step in the readout chain. Detector and readout details are discussed in EP2.

freedom for motion, and thus all optical elements were aligned to them, specifically to focal plane H. We made no attempt to align the two focal planes relative to each other and relied on their common, rigid mechanical construction. We also made no attempt to ensure that pairs of detectors at the two focal planes simultaneously observed the exact same sky location. The combination of a rotating AHWP and wire grid made each focal plane detector an independent polarimeter sensitive to the incident  $I$ ,  $Q$ , and  $U$  Stokes parameters.

The lenses and polarizing grid were mounted on custom-made adjustable supports that gave a dynamic range of 3 mm and  $1^\circ$  in lateral and rotational positions. They were aligned to the focal planes using a portable coordinate measurement machine.<sup>24</sup> The alignment took into account the few millimeters of differential thermal contraction of the receiver elements, including the receiver shells, the Vespel legs that mount the optical elements to the 4 K cold plate, and the PE from which the lenses were made (Zilic 2014).

We transferred the alignment of the internal optics to a reference frame defined by three tooling balls mounted on the cryostat shell near the vacuum window. This reference frame was used to align the secondary mirror to the receiver, and subsequently the primary mirror was aligned to the secondary. The mirrors were mounted to the inner frame of the gondola using custom-built hexapods with a 25 mm lateral and  $3^\circ$  rotational dynamic range. The primary and secondary mirrors each had three tooling balls in known locations relative to the reflector surface. After the initial mounting of the secondary mirror, we used an inside micrometer to measure the nine relative distances between the receiver and secondary tooling balls and compared them to the distances required by the optical design. The repeatability of the inside micrometer’s measurements was 0.075 mm. We used a computer program to calculate the hexapod leg lengths that would bring the mirror to its required position. The hexapod legs were adjusted manually and locked in position, and the distances were remeasured to verify proper alignment. The procedure was repeated for the alignment of the primary mirror relative to the secondary. Post-alignment, the nine distance measurements between the secondary and the receiver (the primary and the secondary)

were between 25 and 175 (25 and 350)  $\mu\text{m}$  from the design values, with an rms of 110 (180)  $\mu\text{m}$ .

The final nine distance measurements were used to recreate the most probable relative positioning of the optics. That geometry was programmed into CodeV, and the beam sizes were compared to the nominal alignment. The 250 and 410 GHz beams were expected to grow by 10%, and there was no change expected for the 150 GHz beams.

### 2.5. Antireflection Coatings

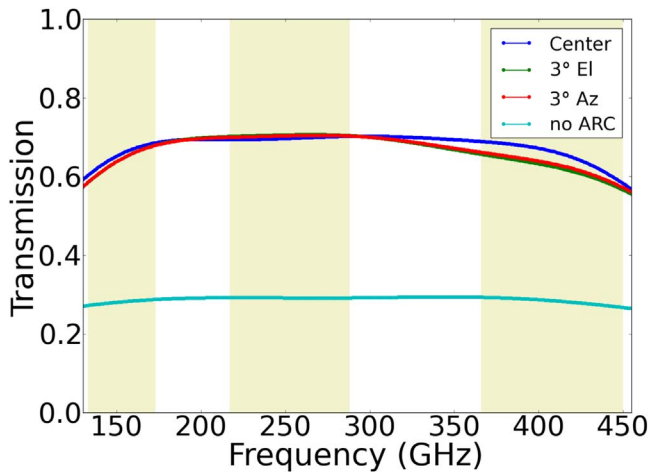
The PE lenses and vacuum window were coated with microporous Teflon<sup>25</sup> to provide a broadband antireflection coating (ARC). The Teflon had an index of refraction  $n = 1.23$ . A 200  $\mu\text{m}$  thick layer was bonded to the sky-facing side of each lens, and a 400  $\mu\text{m}$  thick layer was bonded to the focal plane side. For the vacuum window the thicknesses were 180 and 460  $\mu\text{m}$ , respectively. Figure 5 gives the calculated end-to-end transmission as a function of frequency including all optical elements.

We chose the ARC thicknesses of the porous Teflon by ray-tracing a range of available thicknesses and choosing the combination that produced the lowest instrumental polarization. For each coating option we calculated the cumulative Mueller matrix of the optical system traced from the sky to, but not including, the AHWP. This Mueller matrix was averaged across the entrance pupil and over five frequencies within each band. We choose the ARC that minimized instrumental polarization  $\sqrt{IQ^2 + IU^2}$  at the azimuth extreme of the FOV, where  $IQ$  and  $IU$  are Mueller matrix components. The design provided maximum instrumental polarization at 150, 250, and 410 GHz of 1.2%, 1.8%, and 0.5%, respectively. The instrumental polarization was dominated by the tilt and curvature of the field lens.

The Teflon ARC was heat-bonded to the PE lenses. During this process, the lenses distorted relative to their machined, designed shape. We measured the final lens shapes including the ARC and ray-traced the final optical system. Figure 6 shows the effect on the Strehl ratios; compare to Figure 3. The average change in Strehl ratio was a decrease of 0.02, 0.03, and 0.11 for the 150, 250, and 410 GHz bands, respectively.

<sup>24</sup> Microscribe MX.

<sup>25</sup> Porex, U.K.



**Figure 5.** Total transmission as a function of frequency (red, green, blue) including the ARC applied on the vacuum window, lenses, filters, and AHWP, compared to the transmission without ARC (cyan). We used CodeV to calculate the  $H$  Mueller matrix element at three locations on the focal plane: the center (blue), center top (green), and center right (red). Absorption is not included, as reliable information about the absorption at cryogenic temperatures was not available. The vertical khaki bars show the EBEX frequency bands.

Figure 7 gives the calculated instrumental polarization of the final optical system, including optical elements up to and including the field lens. The field lens was the dominant contributor to instrumental polarization. This is represented by the radial orientation of the polarization vectors and the increase in magnitude with radial distance.

### 2.6. Electromagnetic Filters and Frequency Bands

A set of reflective and absorptive low-pass filters (see Figure 8 and Table 2), together with the horn-array waveguides, were dominant in determining the transmission properties of the instrument. We used metal mesh low-pass filters (Ade et al. 2006) and an absorptive Teflon filter. For ground operations only, a neutral density filter (NDF) was also used.

We used two types of metal mesh low-pass filters, a “thermal” and “low-pass edge (LPE).” The thermal filters were 10  $\mu\text{m}$  thick polypropylene with a copper mesh layer sized to reflect frequencies in the infrared band. The LPE filters were made up of multiple layers of single mesh layers embedded in polypropylene with microporous Teflon (see footnote 25) antireflection coating. Three types of LPE filters were placed sky side of the polarizing grid to reject thermal radiation, and two LPE filters per frequency band were placed on each focal plane to define the high-frequency edge of each of the bands. The 3 dB cutoff for each of these filters is given in Table 2, and the filter transmission curves for the 150 GHz filters are shown in Figure 9. The low-frequency edge of each of the three EBEX frequency bands was set by circular waveguides positioned between the horns and the detector wafers; see Figure 4. The waveguides had diameters of 1.32, 0.81, and 0.48 mm for the 150, 250, and 410 GHz bands, respectively, giving the turn-on frequencies listed in Table 2. The location and cutoff of the high-frequency edge of the bands due to the LPE filters made the  $\text{TE}_{11}$  mode dominant. Convolving the transmission of the LPE filters with the transmission function for the  $\text{TM}_{01}$  mode, which is the next most dominant mode, we find that it contributed 1.4%, 4.2%, and 0.07% for the 150, 250, and

410 GHz, respectively, relative to the  $\text{TE}_{11}$  mode. Contributions from higher modes were negligible.

The absorptive IR filter was a 12.7 mm thick slab of Teflon heat sunk to the liquid nitrogen (LN) stage. We chose Teflon for its low index of refraction and strong infrared but relatively low millimeter-wave absorption. However, because of its low thermal conductance, the central region of the filter reached temperatures of 110 K, making emission from this filter a significant fraction of the total calculated optical load on the detectors; more details are provided in EP2.

For ground work we added an NDF on the focal plane side of the field lens. Without the NDF the atmospheric load during ground testing would saturate the detectors in all bands. The NDF was made from a slab of Eccosorb MF110<sup>26</sup> machined down to produce seven hexagonal segments of different thicknesses. Since the NDF was near a field stop, these seven segments corresponded to the seven wafers on the focal plane. The central section, corresponding to the 410 GHz wafer, was 6.6 mm thick, while the 250 and 150 GHz segments were 10.8 and 18.3 mm thick, respectively. The NDF was coated with a 0.5 mm layer of Teflon. The predicted transmission of the NDF was 1.4%, 1.3%, and 1.6% at the 150, 250, and 410 GHz bands, respectively.

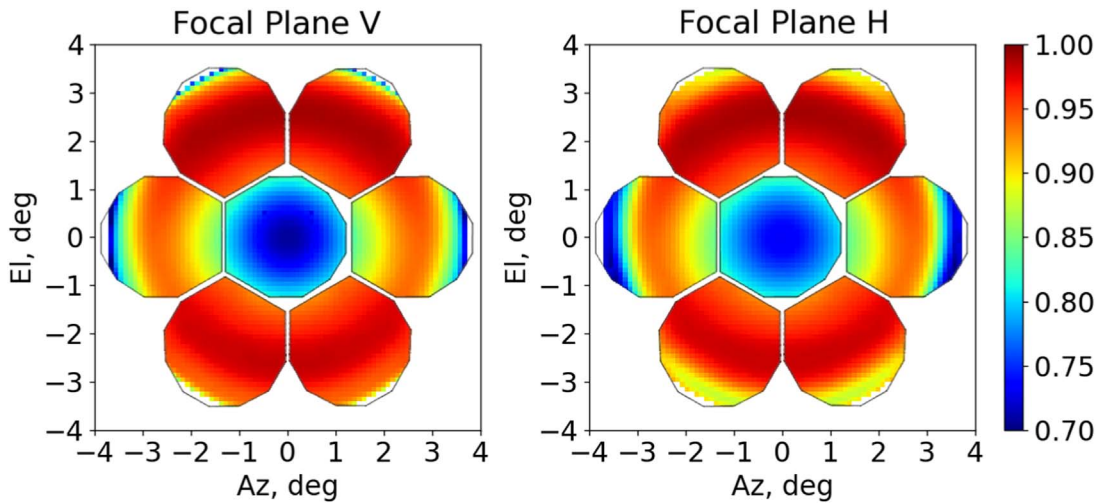
We measured the end-to-end frequency response of the instrument using an Ebert–Fastie spectrometer (Fastie 1952a, 1952b; Polsgrove 2009; Zilic 2014) that had a 1200 K blackbody and a chopper as an input source. The output radiation was coupled to the receiver only—without the warm telescope—specifically to the throughput of individual focal plane detectors using lenses and a fold mirror; see Figure 10. A translation stage was used to couple the spectrometer to between 10 and 12 detectors from each frequency band. The 12 mm exit aperture of the spectrometer gave output frequency bandwidths between 1.3 and 3.0 GHz, 2.4 and 5.1 GHz, and 4.1 and 7.0 GHz for the 150, 250, and 410 GHz bands, respectively. We measured the frequency response of the detectors with a resolution that was approximately half the width of the output bandwidth. For each frequency band we find an average response as a function of frequency by averaging individual spectra weighted by signal-to-noise ratio. We then least-squares minimize the average and the predicted responses with an overall scaling as the only free parameter; during that step, the highest predicted response is normalized to 1. The measured bands are shown in Figure 11 and are interpreted as the end-to-end band shapes because within these narrow bands the ambient temperature mirrors are achromatic.

### 2.7. Beams

Viewed in the time-reversed sense, the focal plane feed horns launch antenna patterns that propagate through the optical system into a far-field pattern on the sky. In addition to the horns, the polarizing grid and the aperture stop are central in determining the far-field shape and size of the beam. The polarizing grid breaks the rotational symmetry of the horn, and therefore the beams are inherently elliptical. As the aperture stop is an image of the primary mirror, the Fourier transform of its illumination gives the far-field pattern.

A rigorous prediction of the far-field antenna pattern requires physical optics calculation including all elements in the optical

<sup>26</sup> Emerson and Cuming Microwave Products, Inc.



**Figure 6.** Strehl ratios at the focal plane as calculated using the measured shape of the lenses after applying the ARC. The change in Strehl differed between the focal planes because each focal plane had a different camera lens.

path. We do not have the capability to carry out this calculation. We make approximate predictions by simulating the antenna pattern of the horn, calculating the shape of its illumination on the stop, and carrying out the Fourier transform to find the far-field beams. To simplify the calculation of the Fourier transform, we use a circularly symmetric Gaussian pattern that is the best fit to the elliptical pattern. The predictions for the illumination on the stop and for the far-field beams are given in Table 3. The table shows that at 150 GHz a significant fraction of the beam is intercepted by the cold stop. This is the main reason we kept the stop at a temperature below that of the sky.

We measured the beam size and shape of the EBEX optical system on the ground and in flight. On the ground we used a tunable (125–140 GHz) Gunn diode with a modulating power source mounted on a water tower that was 50 m high and 104 m horizontal distance from the payload, giving a total distance of 115 m. The source had a wire grid polarizer at the exit aperture to ensure highly polarized emission. For the 150 GHz band measurements the source frequency was set to 140 GHz. We used a doubler and a tripler to set the source to 254 and 410 GHz for the two higher-frequency bands, respectively. We raster-scanned the source while simultaneously rotating the AHWP to make detector time streams that had three modulations: the raster scan period, the rotation of the AHWP, and the on/off modulation of the source. Using the double demodulation analysis technique described in Appendix A, we made intensity maps of the source with a subset of the detectors. We fitted the measured antenna response of each bolometer to a 2D Gaussian and extracted the two FWHMs; Figure 12 shows a beam map for one of the detectors at each frequency band. To give an indication of the average beam per frequency band, Figure 13 shows a signal-to-noise ratio weighted map made from all the beam maps of all detectors at each frequency band. Table 3 gives the measured sizes of the beams. We find that the beams at the higher-frequency bands are larger than the design. We ascribe this difference to the error in index (see Section 2.3) and to a slight misalignment of the telescope, which would affect the higher-frequency bands more than the 150 GHz band.

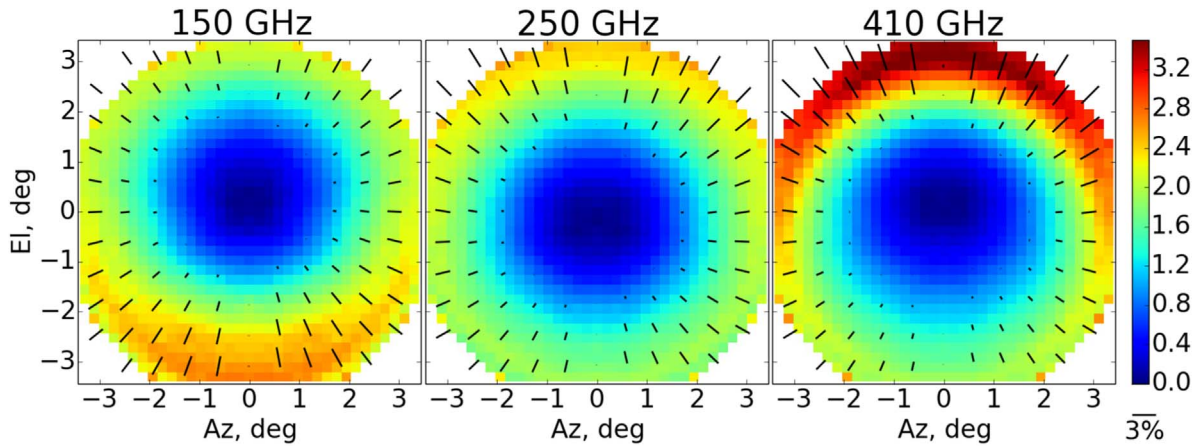
The in-flight beam size is inferred from maps made of passes of the galactic source RCW38. Because of a malfunction with

the azimuth motor, described in EP3, many detectors have only a few passes in the vicinity of the source, and we cannot reliably reconstruct their beam shapes. We therefore construct one effective temperature beam map per frequency band using all detectors for which we have valid absolute calibration. (The absolute calibration is discussed by Aubin et al. 2016.) The 150, 250, and 410 GHz maps use data from 331, 231, and 80 detectors, respectively. The data maps are compared to temperature reference maps that are made with various smoothing scales, as described below. We deduce the beam size from the reference map that best fits the data.

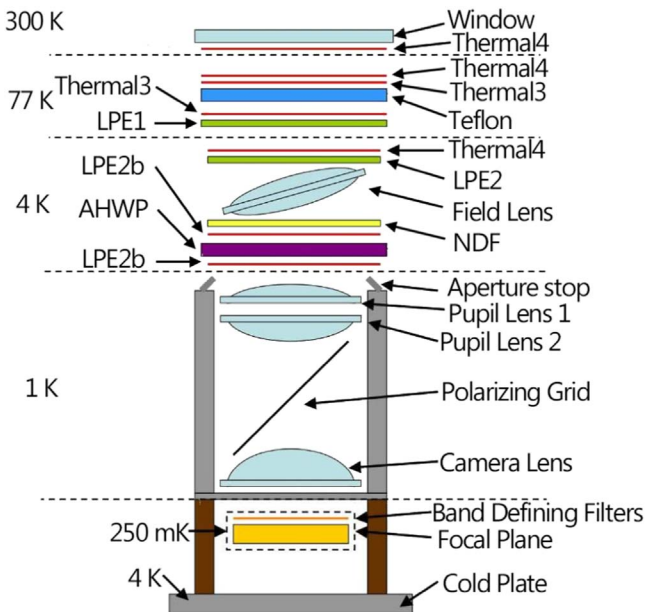
For the 250 and 410 GHz bands we generated the reference temperature maps by summing the component maps, which have been scaled to and integrated over the measured EBEX bands (Planck Collaboration et al. 2016). For the 150 GHz band we used the 143 GHz map. At this frequency the component map reconstructs RCW38 poorly, and the 143 GHz data are sufficiently close to the EBEX 150 GHz band. We made a bank of reference maps by smoothing the temperature map with a 2D symmetric Gaussian to a range of scales from 8 to 40'. The pixelization was 1/7. Using the EBEX2013-EBEX2013 pointing information, we created detector-specific simulated time-ordered data (TOD) by scanning the bank of reference maps. The TOD were subject to the same filtering and processing as the corresponding EBEX2013 flight detector data. We compared the measured data and each of the simulated maps for a square region that is  $1.2 \times 1.2$  around RCW38.

We found in-flight beam sizes of 32, 30, and 30' for the 150, 250, and 410 GHz bands, respectively; see Figure 14. These were larger than beams measured on the ground. There are two possible reasons for this difference: (a) detector pointing uncertainty, and (b) nonoptimal alignment of the telescope. Making combined maps from many detectors requires knowledge of their relative positions on the focal plane with an accuracy much smaller than the inherent beam size, namely, 1–3'. As discussed earlier, we could not use flight data to determine these relative positions for many of the detectors. Instead, we relied on the mechanical design of the focal plane. For a handful of the detectors at 250 GHz for which there were data, there was evidence that this assumption gave offset errors on the order of the beam size, leading to smearing and hence to





**Figure 7.** Magnitude and orientation of calculated instrumental polarization (IP) for the EBEX optics up to and including the field lens. Orientation is indicated by the polarization vectors (black bars). Both the color scale and the length of the polarization vectors give the IP magnitude.



**Figure 8.** Ordering of filters along the optical path and their thermal stages.

larger combined beam maps. The ground beam measurements were conducted before shipping the payload to Antarctica. The short flight season in Antarctica did not allow time to repeat beam pattern measurements after reassembling the payload, and it is possible that telescope alignment was not optimal. Further evidence for this hypothesis is provided by the apparent elliptical shape of RCW38 at the EBEX 150 GHz band; see Figure 14. The *Planck* map of RCW38 at 143 GHz shows a more circularly symmetric shape. We note that it also has a smaller peak temperature. Simulations comparing the symmetric beam smoothing of the map with smoothing using an elliptical Gaussian of the size indicated by the data confirm that the smaller peak amplitude is due to the symmetric smoothing.

### 3. Receiver

The EBEX receiver was designed to contain the cold optical elements, as described in Section 2.3, and to provide sufficient cryogenics for 10 days of flight. In addition to providing appropriate heat-sink temperatures between 0.25 and 4 K for optical elements, detectors, and superconducting quantum

**Table 2**  
List of the Filters Common to the Entire Optical Path and Those Specific for Each Frequency Band

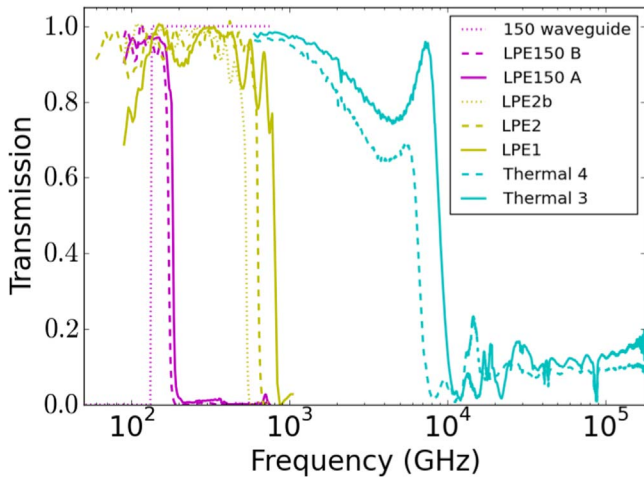
Common Filters		
Name	3 dB (GHz)	
Thermal 3	8930	
Thermal 4	6400	
LPE1	803	
LPE2	631	
LPE2b	531	
Band Filters		
Band (GHz)	Name	3 dB (GHz)
150	LPE150 A	183
	LPE150 B	172
	150 waveguide	133
250	LPE250 A	337
	LPE250 B	285
	250 waveguide	217
410	LPE410 A	558
	LPE410 B	445
	410 waveguide	364

**Note.** The “3 dB” Column gives the 3 dB cutoff and turn-on of the low- and high-pass filters, respectively.

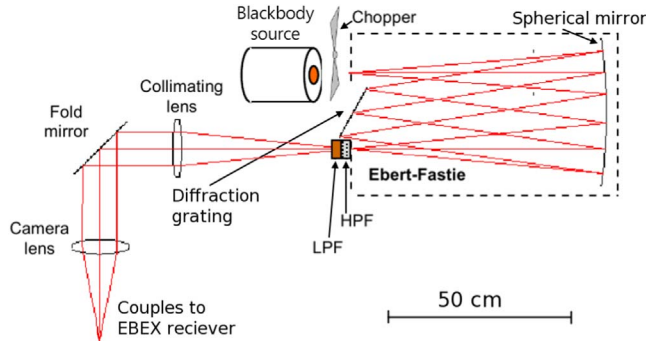
interference device (SQUID) preamplifiers, the design had to implement several features that were unique to this balloon application and to our detector and readout scheme. They include accommodating a double vacuum window mechanism (DVWM), minimizing sensitivity to detector radio frequency (RF) pickup, and reducing as well as characterizing magnetic pickup in detector readout components. These features will be discussed in subsequent subsections.

An overall view of the receiver<sup>27</sup> and its main elements is given in Figure 15. Its bare, dry weight was 642 kg; it was 809 kg including all cryogenics and flight hardware.

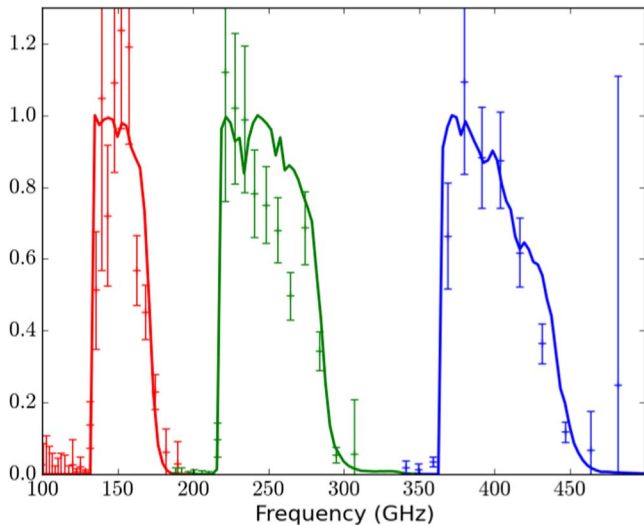
<sup>27</sup> Fabricated by Precision Cryogenics, Inc.



**Figure 9.** Measured transmission curves for the low-pass common filters and, as an example, for the additional band-specific 150 GHz band filters. The high-pass response shown for the 1.32 mm diameter waveguide of the 150 GHz band is based on calculations.



**Figure 10.** Diagram of the spectral response measurement using the Ebert-Fastie spectrometer. The diffraction grating was rotated to send a specific band of frequencies through the exit aperture. At the exit aperture, high- and low-pass filters (HPF, LPF) selected a single diffraction order coming from the grating. The Ebert-Fastie spectrometer was mounted on top of the EBEX receiver (not shown), and two lenses coupled the output to the EBEX optics, illuminating a single detector on the focal plane.



**Figure 11.** Measured (points) and predicted (solid lines) bands at each EBEX frequency. The native measurements were made with higher frequency resolution and were binned to reduce clutter. The predictions are normalized to 1.0.

**Table 3**  
Predicted and Measured Beam FWHM for the Long ( $a$ ) and Short ( $b$ ) Axes

Band (GHz)	Predicted		Measured (')			
	Taper (dB)	FWHM (')	One		Average	
			FWHM $_a$	FWHM $_b$	FWHM $_a$	FWHM $_b$
150	-7.2	7.8	8.6	7.6	8.9	8.3
250	-19.4	5.8	8.2	6.4	7.6	7.4
410	-50.1	5.0	8.6	6.5	11.9	10.1

**Note.** The “One” column gives the parameters for the beams measured for one detector in each frequency band, as shown in Figure 12. The “average” is for a signal-to-noise ratio weighted mean of all the detectors measured per frequency band. The parameters measured are for the long and short FWHM of a 2D Gaussian fit.

### 3.1. Cryogenics

The receiver had eight thermal stages. Five of these stages were provided by the mechanical construction of the cryostat, which included an outer vacuum shell at ambient temperature, a nitrogen vapor-cooled layer that was typically at 180 K, a 130-liter LN reservoir, a helium vapor-cooled layer that was typically at 25 K, and a 130-liter liquid helium (LHe) reservoir; see Figure 15. Three other temperature stages were provided by sub-kelvin refrigerators that will be described below.

During flight, we maintained both LHe and LN near atmospheric pressure using valves<sup>28</sup> that maintained a pressure of  $15.7 \pm 1$  psi. The reservoirs were kept near atmospheric pressure to stabilize the cryogen temperatures at design values and to reduce the boil-off rate of the cryogens. We also had commandable, motorized gate valves<sup>29</sup> to vent the tanks to ambient pressure, if necessary, specifically in case of flight termination before cryogens expired. These were only used when the flight ended, long after the cryogens expired. Table 4 gives the preflight calculated heat loads on the LN and LHe reservoirs. With 130 liters each of LN and LHe, these give a hold time of 11.8 and 10.8 days for LN and LHe, respectively. The LHe cryogen ran out after 10.8 days; we did not monitor the LN hold time.

Cooling to sub-kelvin temperatures was achieved with two closed-cycle, pressurized helium adsorption refrigerators.<sup>30</sup> A two-stage 30 STP liter  $^4\text{He}$  refrigerator cooled the aperture stop and downstream optical elements with the exception of the focal planes. When the AHWP was rotating (stationary), the base temperature was 1.2 (1.0) K, the hold time was 48 (87) hr, and the calculated load was 320 (70)  $\mu\text{W}$ . The source of power dissipation by the AHWP mechanism is discussed in Section 4.3.1. The second most significant source of heat load on the 1 K stage was conduction through the polyimide legs<sup>31</sup> with which the optics box was mounted to the cold plate. A cryogenic stepper motor was used as a mechanical heat switch between cold plate and the optics box during initial cooling of the equipment. This reduced the cool-down period from 12 to 4 days.

Two heat-sink temperatures, 320 and 240 mK, were provided by a three-stage adsorption refrigerator with a  $^4\text{He}$  pre-cooling stage and two  $^3\text{He}$  refrigerators. The focal planes,

<sup>28</sup> Tavco, Inc.

<sup>29</sup> Varian, Inc.

<sup>30</sup> Chase Research Cryogenics, Inc.

<sup>31</sup> Vespel SP-1, Dupont.

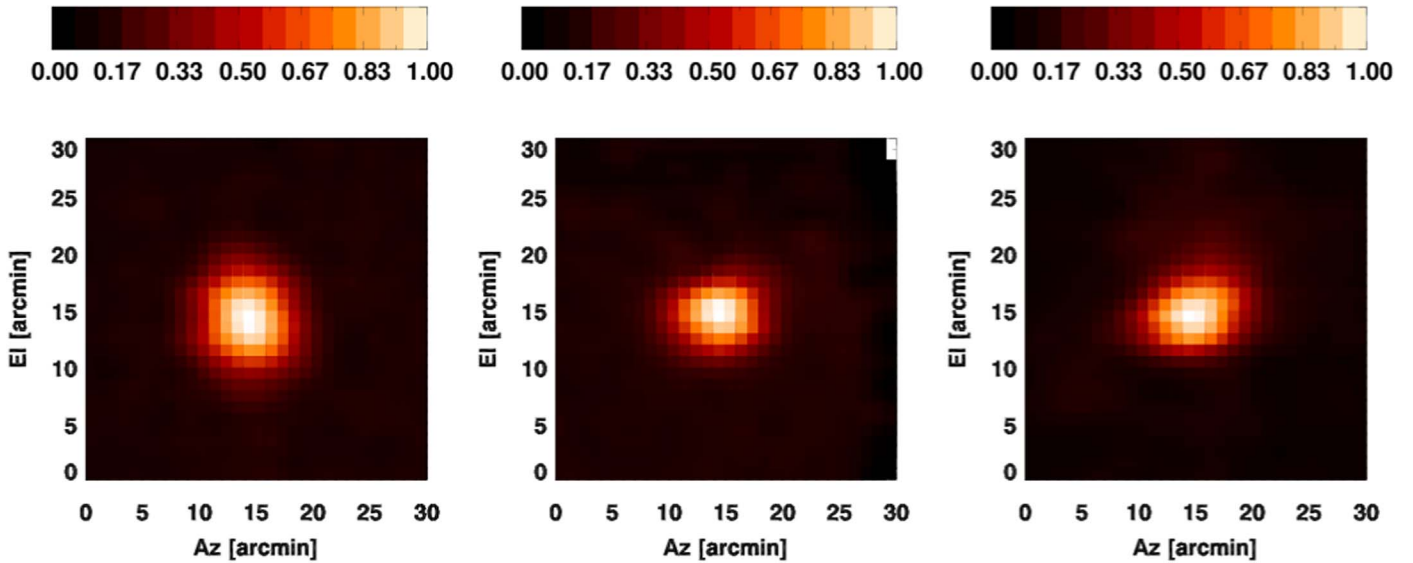


Figure 12. Example ground calibration beam map from one detector for each of the 150 (left), 250 (middle), and 410 GHz (right) frequency bands.

including the detectors and their associated LC boards (see EP2), were operated near 250 mK. Both the 320 mK and 1 K stages were used as heat sinks for wires leading from the focal planes to warmer temperature stages. The refrigerator had 2 STP liters of  $^3\text{He}$ , a total heat load of  $0.5 \mu\text{W}$  on the coldest stage, and a hold time of 84 hr. The heat load on the coldest stage was dominated by a  $0.2 \mu\text{W}$  load owing to detector wiring.

The cryogenic system had temperature stability better than our requirement on gain fluctuations. Temperature fluctuations over a representative period of several hours are shown in Figure 16. The 0.1 mK rms temperature fluctuations produced bolometer gain fluctuations of 0.05%, which were negligible compared to other sources of calibration uncertainties.

### 3.2. Double Vacuum Window Mechanism

At the top of the 300 K shell, a 30 cm open aperture window separated the vacuum environment of the receiver from ambient pressure. Several materials were considered for this vacuum window, including sapphire, zotefoam,<sup>32</sup> polypropylene, and polyethylene. We chose polyethylene (PE) because of the combination of its optical properties, durability, cost, ease of implementation, and the availability of broadband antireflection coating.

We used a 12.7 mm thick PE when operating the receiver in the laboratory. Thinner material would bow inward and (1) deflect and damage the infrared blocking filters that were mounted beneath the window (see Figure 8) and (2) induce instrumental polarization due to differential reflection. Thermal emission from a 12.7 mm thick PE window operating near 300 K, which was a typical receiver shell temperature at float, would have given 30% higher in-band load at 150 GHz compared to the CMB. To reduce this load, we implemented a DVWM that consisted of both the 12.7 mm thick and a thinner window. The mechanism is shown in Figure 17. During ground operations, the thick window was placed above the thin window with the cavity between the windows evacuated to put

the pressure differential of the atmosphere on the thick window. When the payload reached altitude above which the ambient pressure was less than 10 torr, a ground operator commanded a motor that moved the thick window aside, exposing an open aperture above the thin window. The thick window was moved back before flight termination to protect the thinner window from atmospheric pressure.

We conducted deflection tests on 30 cm PE windows to measure the maximum central deflection as a function of window thicknesses and differential pressures; see Figure 18. These tests indicated that at the expected float pressures of up to 10 torr a 1 mm thick PE window would be adequate. A 10 torr pressure differential was considered a conservatively high estimate because it corresponds to an altitude of 28 km. Flight altitude ranged from 34 to 36.5 km. Thermal emission from the thin window was a factor of 10 less than in-band CMB power at 150 GHz.

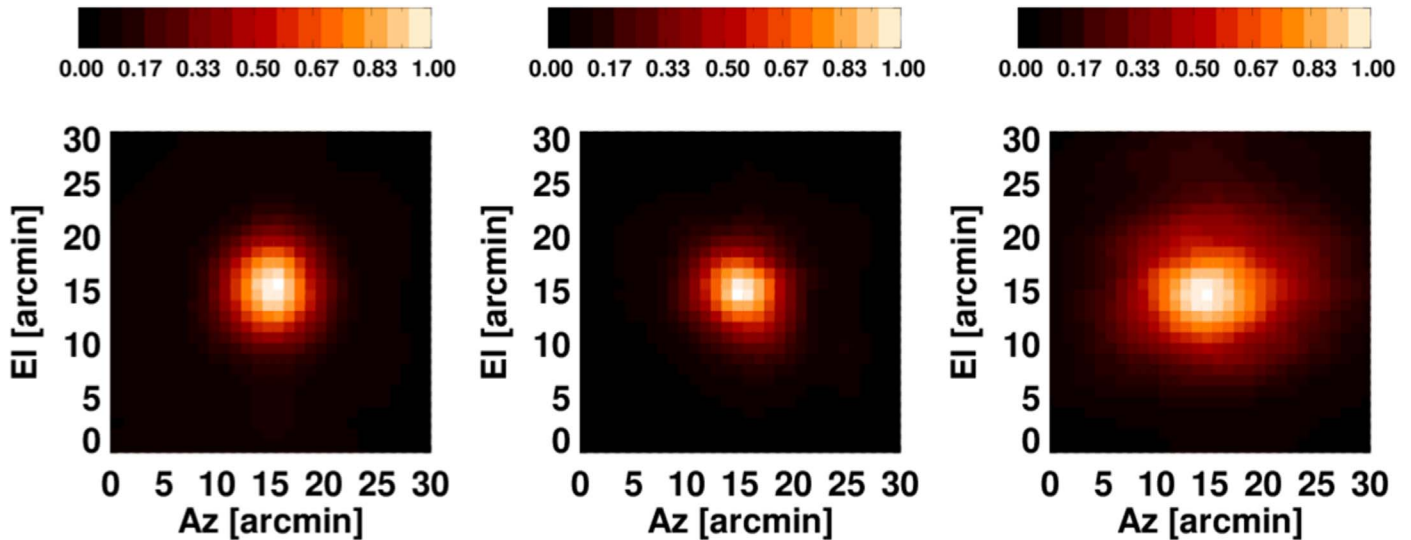
During the EBEX2013 flight, we removed the thick window when the payload ascended through a pressure of 8 torr. The thick window was returned to the optical path after the liquid cryogenics were exhausted, 11 days after launch. In-flight readout of the DVWM position and post-flight inspection indicated nominal operation. The DVWM is described elsewhere in more detail (Zilic et al. 2017).

### 3.3. Mitigation of Radio Frequency Interference

The TES bolometers, the SQUID preamplifiers, and the bias and readout wiring were sensitive to RF electromagnetic waves and were thus susceptible to RF interference (RFI). Columbia Scientific Balloon Facility's radio and video transmitters operating at frequencies between 0.9 and 2.5 GHz were a source of RFI. To mitigate RFI, we constructed an RF-shielded environment that encompassed all the RFI-sensitive equipment. The shielded environment is shaded green in Figure 19.

The majority of the RFI cavity consisted of a Faraday cage provided by metallic walls. It included the receiver's vacuum jacket, a can at the bottom of the cryostat that contained the SQUID controllers, a domestic dryer hose whose metallic shell shielded cables between the receiver and the readout crates, and

<sup>32</sup> Zotefoams, PLC.



**Figure 13.** Signal-to-noise ratio weighted ground calibration beam maps made from beam maps of all detectors of each frequency band (left to right: 150, 250, and 410 GHz).

the walls of the readout crates. Connections between Faraday cage walls had RFI gaskets<sup>33</sup> or relied on closely spaced screws to give a waveguide cutoff below 6 GHz.

The 30 cm diameter vacuum window was many RF wavelengths across, allowing RF radiation to enter the cryostat cavity (red shaded region in Figure 19). The bolometer wafers were protected because they were enclosed in a Faraday cage and because the waveguides between the feed horns and the bolometer cavities acted as high-pass filters. Bolometer wiring passed from the focal planes via “RF towers,” which will be described below, to SQUID amplifiers mounted below the cold plate, and from there through the various cryogenic shells to the 300 K vacuum jacket; see Figure 19. It was therefore important to ensure that the intershell region was RFI free. We prevented RF radiation from entering the cryostat’s intershell region by gluing a 25.4  $\mu\text{m}$  thick stainless steel foil between the cryogenic shells near the vacuum window. The glue was electrically conductive. The additional thermal load imposed by this foil was 1% the total load on the LHe stage and smaller for the warmer stages. The foil’s RF attenuation between 0.9 and 2.5 GHz varied from  $-16$  to  $-26$  dB, respectively.

Between the focal planes and the cold plate of the instrument were two structures, one per focal plane, called “RF towers.” The RF towers provided an RF-clean environment for the wires leading from the focal plane to the SQUID amplifiers while minimizing the thermal conductance between the 0.24 and 4.2 K thermal stages. Each RF tower was a cylinder composed of sections of Vespel<sup>34</sup> tubes interspersed with heat-sink terminals and terminating near the focal planes with a stainless steel bellows. Bolometer wiring passed inside the cylinder. The bellows attached to the Faraday cage surrounding each of the focal planes and facilitated the mechanical connection between a focal plane and its tower despite possible misalignments. The four heat-sink terminals gave thermal connection to the 0.25, 0.33, 1, and 4.2 K stages. An RF-clean environment was maintained inside the RF tower by using a 99.9% purity 5  $\mu\text{m}$  thick niobium foil to completely wrap the Vespel tube through which the wires passed; see Figure 20. The niobium was

purchased in sheets and was wrapped and spot-welded along a vertical seam spanning the length of the RF towers. The welds were spaced every 5 mm for integrity of the seam and rejection of RF frequencies less than 10 GHz. The foil was electrically connected to the metallic ends of each of the heat-sink points using electrically conductive silver-filled adhesive. We used a niobium foil owing to its low thermal conductivity below its 9.5 K superconducting temperature. For our RF tower geometry the heat loads on the 0.25, 0.33, and 1 K temperature stages were 0.06, 2.9, and 41.9  $\mu\text{W}$ , constituting 9%, 18%, and 21%, respectively, of the total load on these stages.

We used commercial capacitive filters<sup>35</sup> for housekeeping wires—such as for temperature sensors and refrigerator control—that crossed the cold plate, which was the boundary between the RFI-contaminated and RFI-clean environments. At room temperature, the filters provided a capacitive coupling between the signal lines of wiring and the system ground with a 3 dB cutoff frequency of 640 kHz and greater than 50 dB attenuation above 1 GHz. We measured the frequency response of the filters at LN and found that the frequency for the 3 dB point increased by a factor of approximately 2. Otherwise, the characteristic shape of the response remained the same as at room temperature. To compensate for the frequency increase of the 3 dB point, we connected two filters in series. We assumed that the measured change is a consequence of thermal contraction of the embedded capacitors and that subsequent contraction to liquid helium temperature was negligible. Similar filters were also applied on wires between the SQUID controllers and the readout crates; they were used as an added precaution.

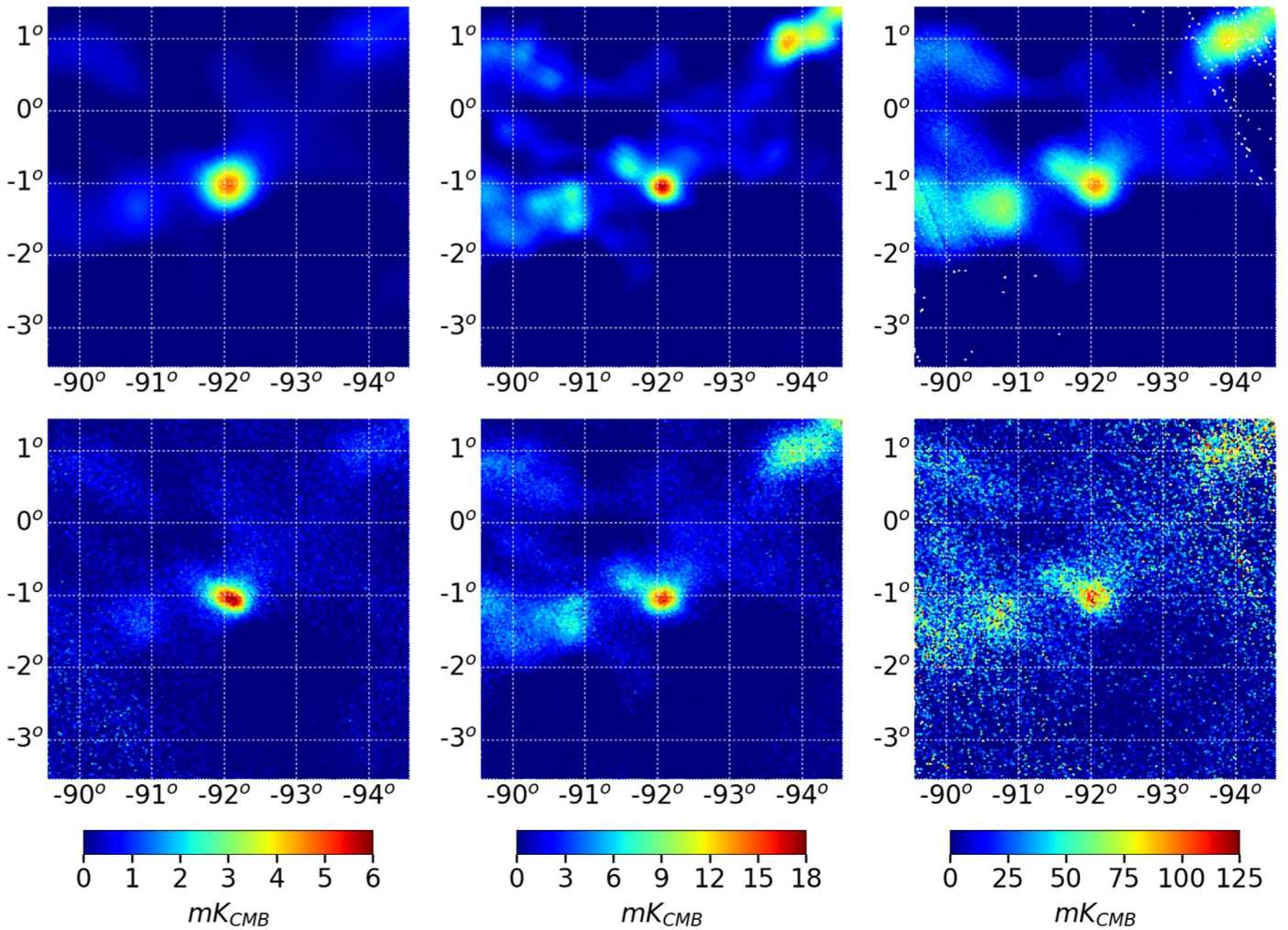
### 3.4. Magnetic Shielding

Both the TES bolometers and the SQUID amplifiers are sensitive to varying magnetic fields. We discuss each in view of the following two sources of time-varying ambient magnetic field: (1) changes in orientation relative to Earth’s magnetic field vector as a function of the azimuthal motion of the gondola, and (2) changes due to the rotation of the magnet on

<sup>33</sup> Parker Hannifin, rectangular strip EMI gasket.

<sup>34</sup> Vespel SP-22, by Dupont.

<sup>35</sup> Spectrum Control.



**Figure 14.** Maps of RCW38 at 150, 250, and 410 GHz (left to right) made by smoothing the data (top row) with symmetric Gaussians. The smoothing scales give the best fits to maps made with data (bottom row) from 331, 231, and 80 detectors at 150, 250, and 410 GHz, respectively. The data indicate that some of the in-flight beams were elliptical; see the text.

which the HWP is mounted because of spatial inhomogeneity in its magnetic field. The rate of variation of both of these sources is at most a few tens of hertz.

### 3.4.1. SQUIDS

Each SQUID was fabricated with an underlying layer of niobium (Huber et al. 2001), and each board with eight SQUIDS was inserted into a magnetic shield,<sup>36</sup> as shown in Figure 21.

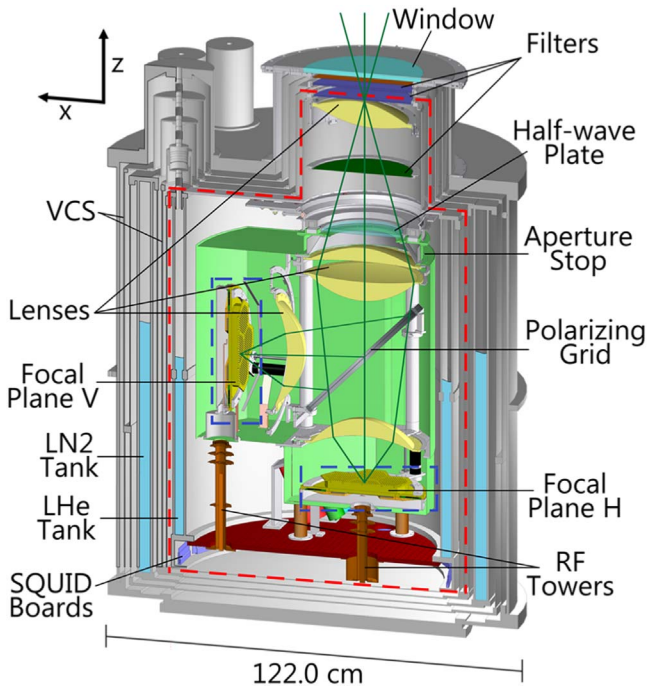
The few tens of hertz magnetic field variation in the sources is much smaller than the standard 0.1–1 MHz readout frequency of the SQUIDS. We therefore do not expect these sources to contribute spurious signals. We searched for azimuth- and HWP rotation-synchronous signals in resistors and in “dark” SQUIDS; these are SQUIDS that were not connected to bolometers but that otherwise shared the same readout path as regular detectors. We binned 6 hr of flight TOD in both gondola azimuth and HWP rotation angle. Neither the raw data nor the binned data show any signature of synchronous signals above the noise.

<sup>36</sup> The MuShield Company Inc.

In addition to the MHz readout frequency that was used for all detectors, we had a readout channel that monitored the SQUID amplifiers at very low frequencies, at and near DC. We did detect variations in Earth’s magnetic field flux passing through the SQUIDS in that readout channel, called “SQUID DC.” This detection is now used to quantify the attenuation of the SQUIDS’ magnetic shielding.

Figure 22 shows data from the SQUID DC channels of three SQUIDS mounted on three different boards. There is a clear sinusoidal modulation at a frequency of one azimuthal rotation. The boards are mounted at different azimuthal angles relative to each other, which is the source of the phase offset between the three data sets. We set the zero angle in the right panel of Figure 22 such that a SQUID board mounted at that angle would be aligned with the orientation of Earth’s magnetic field at the time the data were taken and thus show a phase angle of zero. We measured an offset of  $-8^\circ$  with variance of  $16^\circ$  compared to the best fit. The data support the interpretation of modulation in the signal due to Earth’s magnetic field.

During the 105 minutes of data shown, the horizontal component of Earth’s magnetic field is  $\Phi = 0.103$  G (Thébaud et al. 2015). The attenuation due to the magnetic shielding, defined as the magnetic flux measured with the shielding



**Figure 15.** Electromagnetic radiation (solid green lines) entered the EBEX receiver through a vacuum window and traversed filters, a lens, and the half-wave plate before reaching the aperture stop of the optical system. Two lenses collimated the beam. A polarizing grid transmitted one polarization state to focal plane H and reflected the other to focal plane V. Wires from the focal plane were channeled through Faraday caged “RF towers” to SQUID boards. The focal planes operated near 0.25 K (area enclosed in blue dashed line), most of the internal optics was maintained near 1 K and was enclosed by an absorber-lined metallic shield (shown as green shield), and all components inside of the red dashed line were cooled to liquid helium temperature. Two sub-kelvin refrigerators are not shown.

**Table 4**

Pre-EBEX2013 Calculated Heat Load Contributions to the LN and LHe Stages during Flight

Element	Load on LN (mW) (mW)	Load on LHe (mW) (mW)
Support structure	2260	56
Radiation	12,500	138
Wiring	880	33
AHWP operation (average)	N/A	15
Refrigerator operation (average)	N/A	116
Total	15,640	358

**Note.** Values labeled “average” are the time-average values over the duration of the Antarctic flight based on individual duty cycles.

divided by the flux that would have been measured without, is

$$\epsilon_B = V_{\text{out}} \left( \frac{1}{\Phi_{\text{SQUID}}} \right) \left( \frac{1}{dV/d\Phi} \right) G, \quad (1)$$

where  $V_{\text{out}}$  is the measured SQUID channel voltage,  $\Phi_{\text{SQUID}}$  is the magnetic flux through the SQUID,  $dV/d\Phi$  is the SQUID response function, which is known for each of our SQUIDs, and  $G$  is a known gain factor that depends on the details of the electronics. For 105 SQUIDs we find a mean attenuation of  $1.7 \times 10^{-4}$  with a dispersion of  $0.6 \times 10^{-4}$ .

### 3.4.2. TES Bolometers

We assessed that no protection was necessary for the detectors, and none was provided. The combination of HWP 1.235 Hz rotation speed and design azimuthal scan period of 50 s placed the polarization signals near 5 Hz, far from the tens of millihertz frequency expected from modulation due to Earth’s magnetic field.

The rotation of the HWP itself was very stable (see Section 4.3.1), putting any modulation of the bolometer response due to magnetic field inhomogeneity of the rotor exactly at this frequency and its harmonics. Such signals are degenerate with other rotation-synchronous signals, which are removed during our data analysis process. The characteristics of the EBEX2013 time domain data are discussed in more detail in EP2, Didier (2016), and Raach (2017).

## 4. Polarimetry

EBEX used a combination of a continuously rotating AHWP and a stationary wire grid for its polarimetry. Above a temperature of 30 K thermal emission from the HWP exceeds the power from the CMB. We therefore mounted the AHWP to the 4 K temperature stage. The AHWP was placed approximately 1 cm toward the sky side of the aperture stop of the optical system; see Figure 1. The aperture stop was heat sunk to the 1 K temperature stage; see Figure 24. Tracing the optical path from the sky inward, the AHWP is behind the mirrors, the vacuum window, and the field lens. Thus, the instrumental polarization induced by these elements is modulated by the AHWP and contributes to our observed polarization signal.

### 4.1. Half-wave Plate and Grid

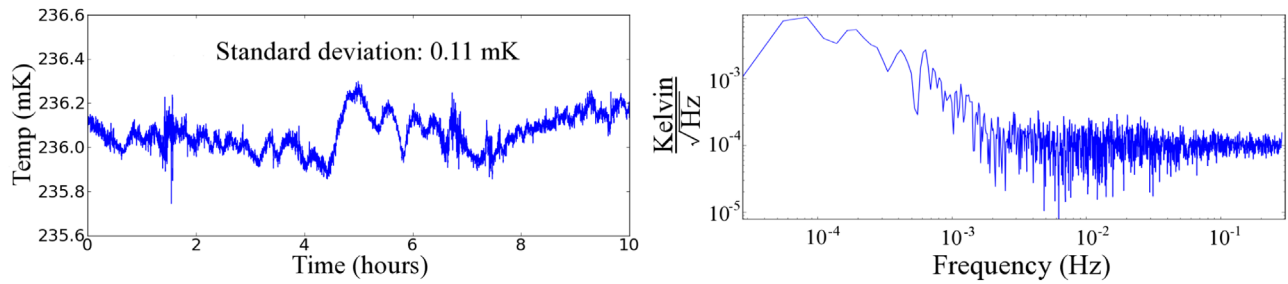
The AHWP was made of a stack of five 24 cm diameter a-cut sapphire disks following a Pancharatnam design (Pancharatnam 1955). The aperture stop diameter was 19 cm. Each of the sapphire plates was approximately 1.66 mm thick, making it a standard HWP for a frequency near 300 GHz. This was near the middle of the broad band required from the AHWP. The thickness of each of the plates is given in Table 5. X-ray diffraction analysis on a smaller, 15 cm diameter a-cut HWP from the same vendor<sup>37</sup> confirmed the crystal orientation and showed a negligible level of defects. The stack is glued by interleaving 12.5  $\mu\text{m}$  thick polyethylene sheets and hot-pressing the entire stack in an oven. The 22 cm diameter ARC consisted of six glued layers per side. Starting from the outermost sapphire plate and listing outward, the layers were Stycast1266,<sup>38</sup> TMM6,<sup>39</sup> Stycast1266, TMM3, 12.5  $\mu\text{m}$  thick polyethylene, and microporous Teflon. The Stycast thickness was approximately 0.025 mm, and the initial thickness of the TMM was 0.38 mm. After gluing with Stycast, each TMM layer was ground to its final thickness. We found that this ARC has survived several cryogenic cycles, although small cracks developed at the outside rim and slowly grew with each cryogenic cycle. Inspection after the EBEX2013 (EBEX2013) flight showed that these cracks did not penetrate the 19 cm optical diameter.

The ordinary and extraordinary axes of each plate were determined by placing the plates between two co-aligned wire

<sup>37</sup> Rubicon Technologies, Inc.

<sup>38</sup> Emerson and Cummings, Inc.

<sup>39</sup> Rogers Corporation.



**Figure 16.** Left: temperature of the coldest stage of the three-stage adsorption refrigerator over 10 hr of the EBEX2013 flight. The 0.11 mK rms temperature stability exceeded the requirement on gain fluctuations. Right: the power spectrum of the temperature fluctuations for the same data section gives a  $1/f$  knee at 2 mHz and is identical to that measured on the detector wafers (not shown). For frequencies higher than 10 mHz, the power spectrum is averaged at constant fractional bandwidth of 0.3%.

grid polarizers and finding minimum transmission at the zero-path difference of a Fourier transform spectrometer. The five plates were then glued, a temporary ARC applied, and the transmission of the stack measured as a function of frequency for 17 stack orientations when placed between two polarizers that were (1) co-aligned, (2) at  $90^\circ$  relative to each other, and (3) at  $45^\circ$  relative to each other. All the data were best fit for individual plate thicknesses and rotation angles. For these fits we assumed the following room temperature indices of refraction  $n$  and absorption coefficients  $\alpha$  for the ordinary ( $o$ ) and extraordinary axes ( $e$ ) (Savini et al. 2006):

$$\begin{aligned} n_o &= 3.053 + 1.4 \cdot 10^{-4}\nu + 2 \cdot 10^{-7}\nu^2 + 3 \cdot 10^{-8}\nu^3 \\ \alpha_o &= 5.2 \cdot 10^{-3}\nu + 5.5 \cdot 10^{-4}\nu^2 + 8 \cdot 10^{-6}\nu^3 \\ n_e &= 3.387 + 4 \cdot 10^{-4}\nu^2 \\ \alpha_e &= 5.2 \cdot 10^{-4}\nu^{2.2}, \end{aligned}$$

where the frequency  $\nu$  is in  $\text{cm}^{-1}$ . These measurements were reported by Matsumura et al. (2009), and the results are given in Table 5. Extrapolating the absorption values to 80 K (Moncelsi et al. 2014), the absorption of the AHWP stack is expected to be less than 0.7% at all frequency bands.

After the final ARC was applied, we again measured the end-to-end transmission of the AHWP as a function of frequency, this time for three relative orientations of the *two polarizers*, and for each of these orientations at every  $5^\circ$  for the AHWP. The three polarizers' orientations were (1) polarizers' transmission axes co-aligned, (2) at  $45^\circ$  to each other, and (3) at  $90^\circ$  to each other (see also Savini et al. 2006, 2009; Moncelsi et al. 2014). The measurements were done at room temperature. The effective ordinary axis for a broadband radiation with a low-pass cutoff at 600 GHz is marked on the side of the stack and is later used for alignment and inside the EBEX receiver. Using the transmission measurements, we calculated the predicted Mueller matrix elements as a function of frequency and polarization modulation efficiency (PME) per band assuming top hat band shapes. We find average PME that are larger than 90% for all three bands, giving a total fractional bandwidth of 109%. Section 4.4 discusses the calibration of polarization rotation and measurements of the PME with the receiver.

A 45 cm inner diameter wire grid is used to analyze the polarization information modulated by AHWP. The plane of the grid is oriented at  $45^\circ$  to the incident radiation such that radiation linearly polarized in one direction is reflected to the V focal plane and radiation polarized in the orthogonal direction is transmitted to the H focal plane; see Figure 15. The wire grid is made by photo-lithographing 400 nm thick copper lines on

$2.5 \mu\text{m}$  thick mylar. The lines have a pitch of  $20 \mu\text{m}$  with  $10 \mu\text{m}$  wire spacing. The transmission of the grid for radiation parallel (perpendicular) to the transmission axis was measured to be larger than 98.7% (less than 0.14%) in the EBEX bands.

The transmission axis of the grid is determined by using a microscope to find the orientation of the lithographed lines relative to the grid holder. The error in this measurement is  $0^\circ.25$ .

#### 4.2. Continuous Rotation Mechanism

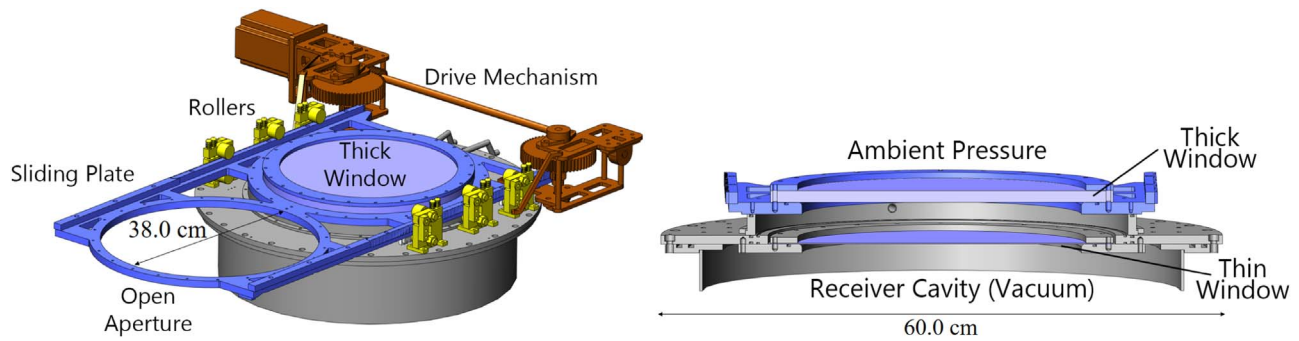
We considered using various types of mechanical bearing systems to achieve continuous rotation. They included small- and large-diameter stainless steel ball bearings, needle bearings with ceramics, and bearings made of special materials such as Teflon and Vespel. We had two requirements for a successful implementation: (1) low-power dissipation, where low was defined as 10% or less of the 360 mW total power load on the liquid helium stage, and (2) HWP rotation lifetime exceeding 2 million rotations at cryogenic temperatures without significant wear and tear to sustain the entire long-duration flight at rotation rates of up to 2 Hz including margin. Available information about friction and experimental testing indicated that none of the mechanical systems we considered satisfied both requirements when considering the size and weight of the EBEX rotor. Mechanical bearing failure due to wear and tear invariably resulted in a sharp increase in power dissipation. We thus chose a high-temperature SMB that provided a no-wear, microphonics-quiet, and relatively low power dissipation rotation.

Hanany et al. (2003) proposed using an SMB for continuous rotation of an HWP and demonstrated a prototype system. Additional papers present the characterization of the coefficient of friction, vibrational amplitudes, resonant frequencies, and sources of power dissipation (Hull et al. 1994; Matsumura 2006) and discuss the implementation of this system in the EBEX 2010 North American test flight (Klein et al. 2011). In this section we review the EBEX2013 implementation (see also Klein 2014). Figures 23 and 24 give a functional sketch and details of the technical implementation, respectively.

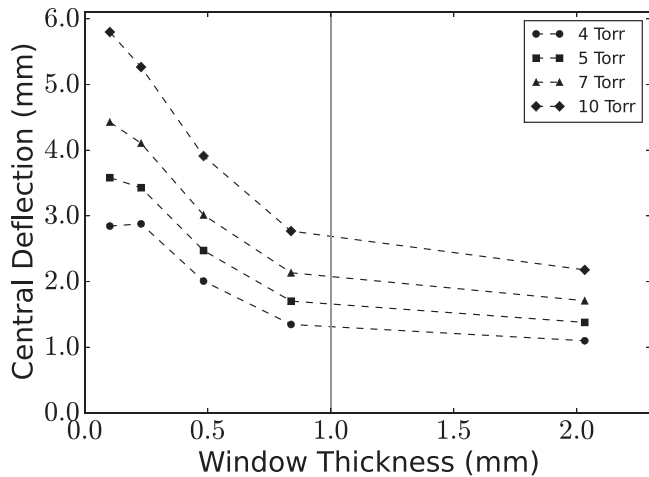
##### 4.2.1. Superconducting Magnetic Bearing

The SMB consisted of a stator made of tiles of YBCO and a rotor made of segments of NdFeB magnet.<sup>40</sup> The stator is heat sunk to the liquid helium bath. It is made of 33 tiles that are glued into a ring with inside and outside diameters of 271 and

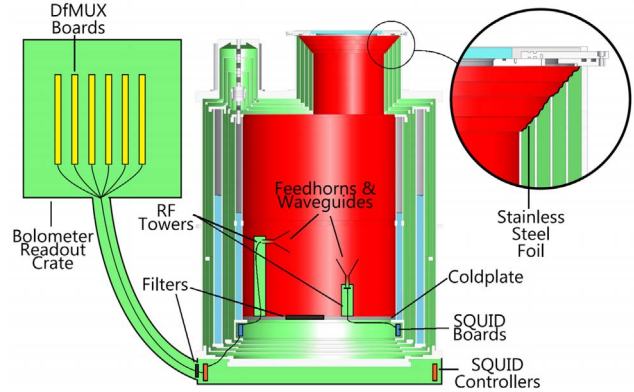
<sup>40</sup> Adelwitz Technologiezentrum GmbH, Germany.



**Figure 17.** Components of the double vacuum window mechanism. The open aperture and thick window on the sliding plate are moved along roller assemblies by a stepper motor drive mechanism. The thick window was placed above the thin window in ground operations.



**Figure 18.** Central deflection of a 30 cm diameter polyethylene window supported at the edge as a function of window thickness under various differential pressures. For EBEX2013 we chose a thin window thickness of 1 mm (vertical solid line).



**Figure 19.** Mitigation against RF contamination relied on filtering and a Faraday cage for the SQUIDS, wires, and electronic boards. We glued stainless steel foil between different cryogenic shells near the vacuum window (zoom-in at top right) to prevent RF radiation from entering the intershell region of the cryostat. Waveguides at the back of the feed horns in the focal plane provided high-pass filtering. The Faraday cage consisted of the walls of the cryostat, the SQUID controller can, a dryer hose, and the walls of the readout crates. Filters, shown on the cold plate and near the SQUID controllers, were installed on individual wires.

331 mm, respectively. The entire ring is glued into a G10 FR4 glass epoxy composite (G10) holder.

The ring-shaped rotor was made of two layers, each of eight arc sections that were stacked brick-like on top of each other. The inside and outside diameters were 284 and 316 mm, respectively, and the total height was 16 mm. All sections were glued into a G10 holder. The axial mean field at 5 mm distance from the surface at the mean radius was  $2.1 \pm 0.1$  kG. The AHWP was mounted to the rotor with an aluminum holder. A wavy washer and an indium wire enhanced the thermal contact between the HWP and the holder. The aluminum holder also had a slotted baffle that was painted with highly emissive material to increase the radiative coupling between the rotor and other receiver cold surfaces (Bock et al. 1995). It was slotted to eliminate eddy currents induced by inhomogeneities in the magnetic field frozen into the superconductor stator. The overall mass of the rotor, including HWP, magnet, and frame, was 5.6 kg, and the moment of inertia was  $0.11 \text{ kg m}^2$ .

#### 4.2.2. Warm Support and Drive Mechanism

At temperatures above 95 K the rotor was held 3.2 mm above the superconductor by a warm support mechanism consisting of three aluminum linear motion grippers. Each gripper was mounted on two parallel, free-motion, linear stages

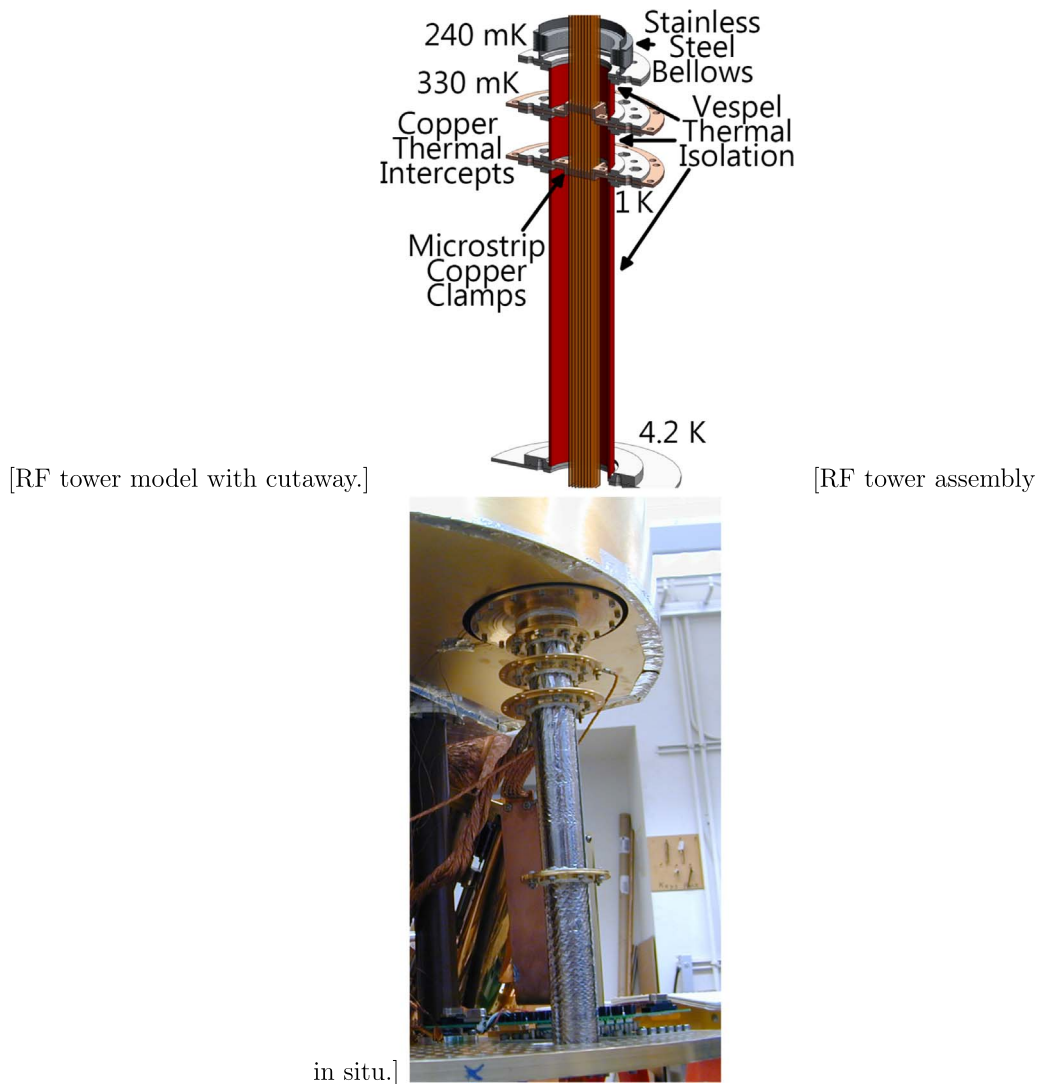
and was pushed into the rotor by a spring. At temperatures below the YBCO critical temperature we pulled the grippers to let the rotor levitate above the stator. For the pulling we used a linear actuator that was connected with kevlar strings to all the grippers; see Figure 23. The actuator maintained its last position when its power was turned off.

The rotor was driven with a belt made of 2.5 cm wide Kevlar tape. The belt connected the rotor to a pulley. The pulley was driven by a thin, hollow, low thermal conductance shaft that extended to the outside of the cryostat and coupled to a DC brushless motor. We used a ferrofluidic vacuum feedthrough at the vacuum jacket of the cryostat.<sup>41</sup> Inside the cryostat the drive shaft was coupled to the helium vapor-cooled shield and to the liquid helium stage using two extra-clearance, molybdenum disulfide dry lubricated stainless steel ball bearings. A tensioner pulley that was mounted with the same type of bearing was used to maintain belt tension. Over the EBEX2013 flight these bearings withstood over 1.5 million rotations with no evidence of failure.

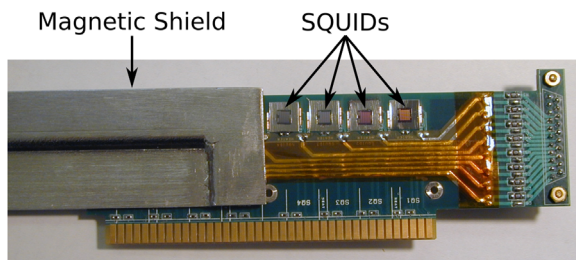
To achieve steady-state rotation, we used two commandable settings for the DC motor, an initial low-speed and a final higher-speed setting. The initial 0.5 Hz low speed was a binary

<sup>41</sup> Ferrotec.





**Figure 20.** RF tower model with cutaway to show interior microstrip assemblies and in situ picture. The RF tower shown in situ was for the V focal plane and has additional length to reduce thermal conductive loading.



**Figure 21.** SQUID board with eight SQUIDs (four visible) and a magnetic shield.

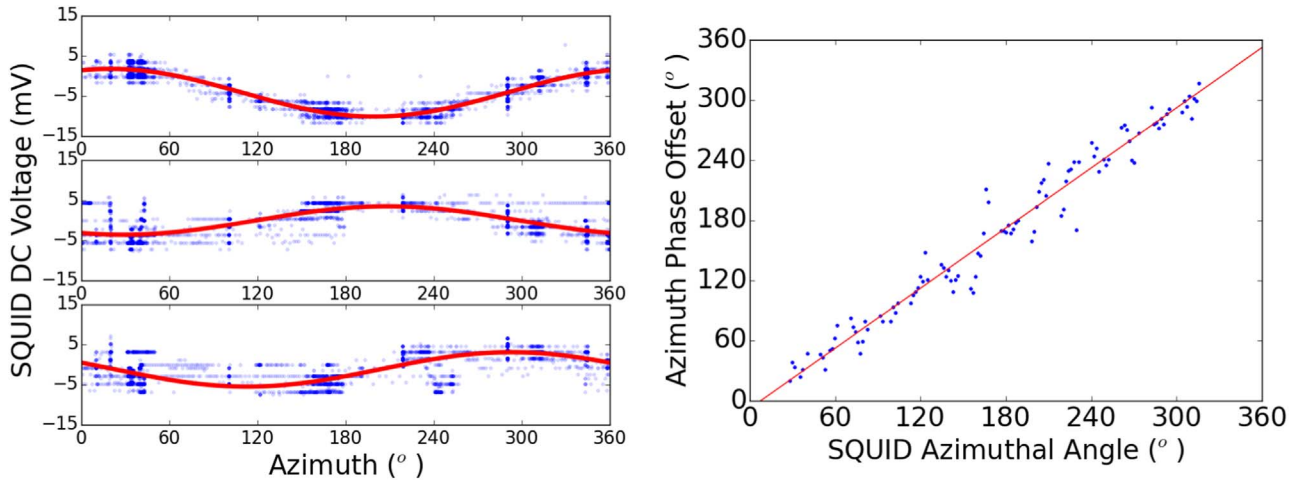
on/off state. When angular encoding showed the rotor rotating stably in its slow mode, we commanded the higher-speed state, which triggered an RC ramp circuit with a time constant of 1 minute that gradually increased the voltage to the motor.

### 4.3. Rotation Angle Encoding and Decoding

We encoded the HWP angular position using a chopper wheel with 240 slots that interrupted a white LED shining onto a photodiode. One of the slots was double width and marked an

arbitrary zero position that was referenced to the ordinary axis of the AHWP. The signals from the photodiode were sufficiently large for angle reconstruction when the LED consumed only  $34 \mu\text{W}$ .

A DfMUX board of the same type used to gather bolometer data recorded and time-stamped the photodiode signals. The sampling rate was 3 kHz, 16 times higher than that of bolometer data. The time domain data of the angle readout was a sinusoidal wave to a good approximation; see Figure 25. We reconstructed the angle by removing an offset and a gradient for sections that were approximately 1 hr long and then identifying times of zero-level crossings. Each zero crossing was assigned an incremental angle of  $0.75^\circ$ . Each bolometer sample has its own time stamp and is associated with an angle by interpolating adjacent time-stamped angles. We constructed an end-to-end simulation of the angle reconstruction that included typical photodiode signal and noise, slot machining errors, and HWP speed variations. A histogram of angle reconstruction errors gives a standard deviation of  $0.01^\circ$ , making angle reconstruction a negligible contributor to the total uncertainty of the polarization angle calibration; see Figure 25 and Section 4.4.



**Figure 22.** Left: SQUID output DC voltage measured as a function of the payload azimuth (blue dots) and a cosine fit (red solid lines) for SQUIDs mounted at azimuthal angle  $28^\circ$  (top),  $203^\circ$  (middle), and  $282^\circ$  (bottom) relative to the orientation of Earth’s magnetic field. More intense data points indicate more data in the specific azimuth and voltage bin. Right: measured phases of the sinusoidal fits shown on the left for 105 SQUIDs (dots). Zero angle is set to align with Earth’s magnetic field at the time the data were recorded. The best-fit offset of a line with unity slope (red) is  $-8^\circ$ ; the variance about the fit is  $16^\circ$ .

**Table 5**  
Parameters of the EBEX Five-stack Sapphire AHPW

Mean Plate Thickness (mm)	Plate Thickness SD (mm)	Fitted Plate Thickness (mm)	Fitted Relative Orientation (deg)
1.655	0.016	1.665	0
1.657	0.015	1.677	26.5
1.647	0.013	1.648	94.8
1.657	0.013	1.675	28.1
1.636	0.017	1.640	-2.6

**Note.** For each plate, the thickness was measured at room temperature in 80 locations. The first and second columns give the mean and standard deviation (SD), respectively. The thermal contraction of sapphire between room and cryogenic temperatures is less than 0.1%. After the five-stack was constructed, we fit spectroscopy measurements to a model in which the thicknesses and relative orientations of the plates were allowed to vary; see text. Here we give the best-fit values (right two columns).

**Table 6**  
Phase Shift due to the Achromatic Nature of the AHPW, for Each of the Calibration Test Setups

Frequency Band	Receiver-only Test	End-to-end Calibration
150 GHz	2°8	2°6
250 GHz	10°4	10°6
410 GHz	2°9	3°5

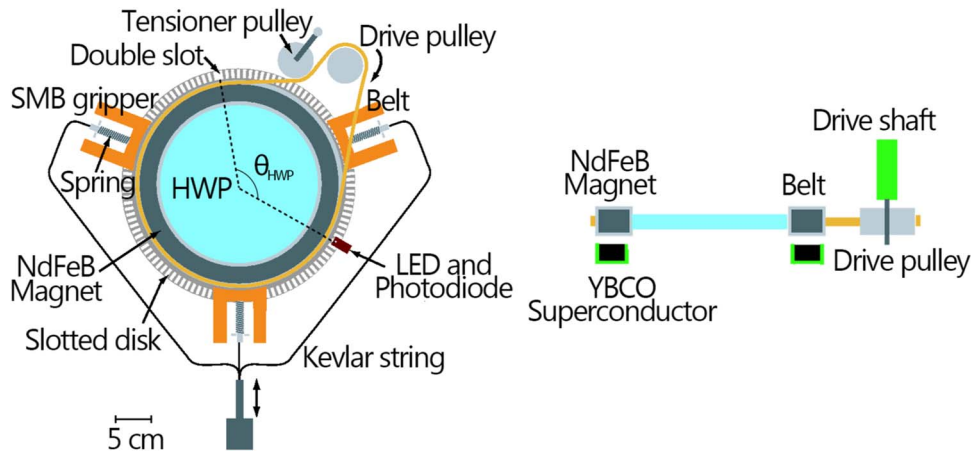
#### 4.3.1. EBEX2013 Operation and Performance

For the EBEX2013 flight we released the warm support and set the AHPW rotating at a frequency of 1.235 Hz well before payload launch. It continued to rotate without interruption through launch. The rotation was stopped and started several times during flight, but the warm support was re-engaged only after liquid helium was exhausted. Over the duration of the flight the rotor executed 584,000 rotations at the nominal rotation speed. The total number of rotations is slightly higher because we exclude a duration of about 4 hr that includes periods during which the speed ramps up to or down from the nominal rotation speed.

Figure 26 shows angle reconstruction over a period of 56 minutes that was stacked rotation by rotation and averaged. A linear increase between  $0^\circ$  and  $360^\circ$  was subtracted. The deviations displayed are the result of speed variations that were repeatable over many rotations. The most prominent deviation had a period of one rotation and was likely due to an overall dipole structure in the strength of the magnetic field between the rotor and stator. This period also gave rise to the largest-amplitude peak in the power spectrum of the rotation rate, as shown in Figure 27. The sawtooth structure shown in the inset of Figure 26 arises from the erroneous assumption during the angle reconstruction that each zero crossing corresponds to exactly  $0^\circ.75$ . The construction of the chopper wheel and the alignment of the LED/photodiode gave closed areas that were systematically slightly larger than the open ones; thus, the assumption that each zero crossing corresponds to  $0^\circ.75$  gave a reconstructed angle per slot that was wrong by less than  $0^\circ.005$ . We did not attempt to correct for this error, which was negligible compared to other uncertainties.

The rotation rate of the SMB extracted from the reconstructed angle gives rms speed variations of 1.5% over a period of 10 hr. This level decreases to 0.45% when we first average the reconstructed angle over a full chopper slot period, namely, over  $1^\circ.5$ , thus eliminating the  $0^\circ.005$  systematic error in angle reconstruction discussed in the previous paragraph. Analysis of the data shown in Figure 27 reveals that 80% of the rms speed variations are due to broadband readout and mechanical noise, rather than specific system resonances. The speed variation at frequencies near 0.1 Hz is much slower than the rotation rate of the rotor, and we hypothesize that these variations are due to a torsional mode of the thin drive shaft. Figure 27 also shows high- $Q$  peaks at harmonics of the rotational frequency and others at  $0.91 \cdot j$  ( $j = 1, 2, 3, \dots$ ) Hz peaks, but the high  $Q$  suggests that these are not due to the tensioner pulley.

Preflight measurements indicated that the power dissipation at 1.2 Hz was 15 mW and that approximately half of that power came from Joule heating due to eddy currents and half due to friction in the Kevlar belt and bearings of the



**Figure 23.** Top (left) and side (right) views of the SMB system. At temperatures below 95 K the rotor, made of NdFeB magnets, and the HWP levitate above the stator, made of YBCO superconductor tiles. A kevlar belt transfers the motion of a drive pulley to the rotor. A tensioner pulley keeps the kevlar tensioned. The drive pulley is coupled to a motor external to the cryostat. Three spring-loaded mechanical grippers support the rotor at temperatures above 95 K. They are connected with kevlar strings to a linear actuator. A combination of a disk with slots, an LED, and a photodiode are used to encode rotational position.

pulleys (Klein 2014). This estimate of total power dissipation proved accurate, as the in-flight total liquid helium hold time matched predictions to within 2%.

#### 4.4. Polarization Calibration

The TOD of a noiseless instrument with a combination of continuously rotating HWP and wire grid analyzer is

$$D(t) = \frac{1}{2}[I + \epsilon Q \cos(4\gamma(t) - \Phi) + \epsilon U \sin(4\gamma(t) - \Phi)], \quad (2)$$

where the incident polarized radiation has Stokes vector parameters  $I$ ,  $Q$ , and  $U$ ,  $\epsilon$  is the PME,  $\gamma = \omega_{\text{hwp}}t$  is the instantaneous angle of the HWP,  $\omega_{\text{hwp}} = 2\pi f_{\text{hwp}}$  is the rotation rate of the HWP, and  $\Phi$  is an overall offset that encodes the angle between the orientation that defines  $\gamma = 0$  and a frame that defines the  $Q$ ,  $U$  coordinate system. In EBEX,  $\gamma$  is the angle between the double slot of the angle encoder and its LED;  $\gamma = 0$  is when the double slot is illuminated. For  $Q$ ,  $U$  it is typical to use either a frame that is locked to the instrument or one that is locked to the celestial sphere. The EBEX polarization calibration relied only on ground-based measurements, as there were no bright astrophysical millimeter-wave sources with sufficiently high polarization to use as calibrators during flight. Therefore, for the calibration we used a  $Q$ ,  $U$  system that is referenced to the instrument. The orientation  $+Q$  was in the symmetry plane of the optical system, perpendicular to the optical axis of the receiver, and aligned with the  $x$  direction shown in Figure 1. The  $+U$  direction is at  $+45^\circ$  relative to  $Q$  (positive angles follow the right-hand rule). Calibration of the instrumental polarimetric response consists of determining the offset angle  $\Phi$  (see Section 4.4.1) and the PME  $\epsilon$  (see Section 4.4.2).

Equation (2) is idealized. It neglects instrumental polarization and ignores spurious input Stokes vectors. Adding these

elements, Equation (2) becomes

$$D(t) = \frac{1}{2}[I + \epsilon Q \cos(4\gamma(t) - \Phi) + \epsilon U \sin(4\gamma(t) - \Phi)] + \sum_{j=0}^{j=\infty} A_j \cos(j\gamma(t) + \phi_j). \quad (3)$$

We have lumped all spurious effects into the coefficients  $A_j$  and phases  $\phi_j$  and phenomenologically allowed them to be present at all harmonics of the rotation frequency. In practice, the first few terms in the expansion are dominant, and we find that they vary with time on timescales slow compared to the rotation rate.

##### 4.4.1. Polarization Rotation

Calibrating the polarization rotation consists of illuminating the experiment with nearly 100% linearly polarized light of known orientation, expressible as  $\alpha_{\text{in}} = (1/2) \arctan(U/Q)$ , and determining  $\Phi$  from the TOD. We used a standard lock-in technique. Multiplying Equation (3) by  $\cos(4\gamma)$  and  $\sin(4\gamma)$  and low-passing to keep only the terms at zero frequency gives

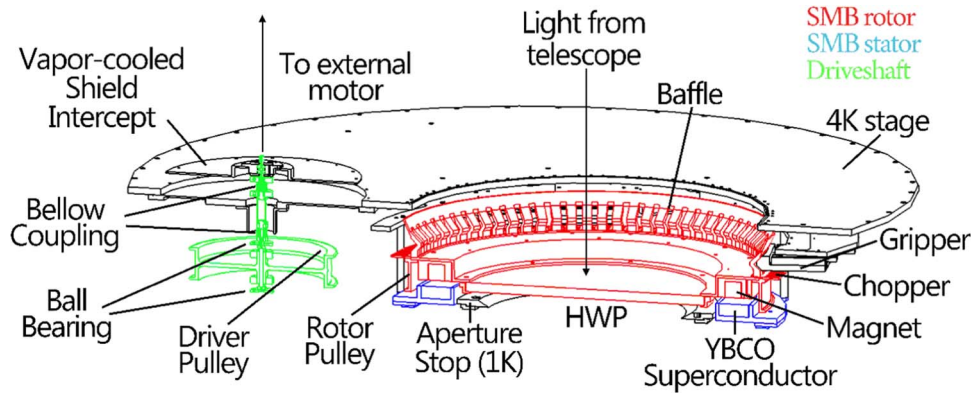
$$D \cos(4\gamma) = \frac{\epsilon}{4} \left( \frac{Q}{\cos(2\alpha_{\text{in}})} \right) \cos(2\alpha_{\text{in}} + \Phi) + A_4 \cos(\phi_4) \quad (4)$$

$$D \sin(4\gamma) = \frac{\epsilon}{4} \left( \frac{Q}{\cos(2\alpha_{\text{in}})} \right) \sin(2\alpha_{\text{in}} + \Phi) - A_4 \sin(\phi_4). \quad (5)$$

The spurious term characterized by  $A_4$  and  $\phi_4$  represents, for example, incident polarization other than the intended source. Without it we readily have

$$\Phi = \arctan \left( \frac{D \sin(4\gamma)}{D \cos(4\gamma)} \right) - 2\alpha_{\text{in}}. \quad (6)$$

To discriminate against spurious polarization signals, we temporally modulated (aka ‘‘chopped’’) the source at frequency  $\omega_c = 2\pi f_c$ ; in reference to Equation (3),  $I$ ,  $Q$ , and  $U$  where



**Figure 24.** Cutaway of the implementation of the SMB with color coding for the different functional elements. The drive pulley and shaft are shown in green, rotating elements (the SMB magnet, HWP, holder, and baffle) in red, and the SMB stator (the YBCO superconductor tiles and holder) in blue.

chopped, but the term  $A_4$  was not. The HWP was rotating continuously at frequency  $\omega_{\text{hwp}}$ . The combination of the temporal modulation of the polarized source and the continuous rotation of the HWP placed the polarization signals of interest at two sidebands of  $4\omega_{\text{hwp}}$ :  $4\omega_{\text{hwp}} + \omega_c$  and  $4\omega_{\text{hwp}} - \omega_c$ . We used a *double* demodulation technique to reject the spurious polarization. We describe the double demodulation technique in Appendix A and show how it gives Equation (6). The bolometer response time  $\tau$  introduced a phase shift between the recorded and input orientation of a polarized signal. We corrected for the time constant by estimating each bolometer’s time constant  $\tau$  and deconvolving the TOD using a single-pole filter response. The process of time constant estimation and deconvolution is described in Appendix B. Detailed time constant measurements showed that a single-pole filter model is only approximate and introduces a bias in the determination of  $\Phi$ . We determined the bias  $\delta\Phi$  using simulations, as described in Appendix B. We report a measured  $\Phi$  that already includes this bias correction.

We measured the angle  $\Phi$  using two configurations: a configuration with only the receiver (without the warm telescope), which we call “receiver only,” and a configuration with the entire instrument including the warm telescope, to which we refer as “end-to-end.” For the receiver-only calibration, a wire grid polarizer was mounted to the vacuum window of the cryostat. The signal to the detectors was modulated between a room-temperature chopper blade blackened with Eccosorb LS140 and a Styrofoam bucket containing Eccosorb CV3<sup>42</sup> and LN that filled the light throughput entering the receiver. Measurements of the orientation of the wire grid transmission axis gave the orientation of the incident polarization to better than  $0^\circ.1$ .

For the end-to-end calibration we positioned a coherent source atop a 50 m tower that was 104 m away from the payload. The source was chopped on/off electronically, and a polarizing wire grid was placed at the output of the horn so as not to rely on its polarization properties. The entire instrument, including receiver, warm telescope, and gondola, scanned the source to construct antenna patterns of the telescope. We determined the relative orientation of the source and telescope by measuring the orientation of each relative to the gravitational acceleration vector using commercial tiltmeters. The

transmission axis of the polarizing grid was aligned parallel to the symmetry plane of the optical system to within  $0^\circ.1$ , giving input polarized light aligned with  $+Q$  in our reference frame.

The measured values of  $\Phi$  for the calibrations are shown in Figure 28. Since the receiver-only calibration used a broadband source, the data shown are an average over the band. For the calibration with the entire instrument we used a coherent source, and the data are valid only at the frequencies shown. The error bars are the standard deviations of the values measured among different detectors of a given frequency band. For the receiver only (end-to-end) we measured 100, 22, and 69 (42, 56, and 151) detectors for the 150, 250, and 410 GHz bands, respectively.

We also used the Ebert–Fastie spectrometer described in Section 2.6 to ascertain that the change in the phase  $\Phi$  *within* each band matched predictions. We placed a wire grid polarizer at the output of the spectrometer. Using the double demodulation technique described in Appendix A, we extracted a phase angle  $\phi$  as a function of frequency  $\nu$ . We only measured the variation of  $\phi(\nu)$  within a band; we did not attempt to determine an offset that would determine  $\phi(\nu)$  relative to  $\Phi(\nu)$ . The data are shown in Figure 28; predictions and measurement are in agreement when the data of each band are given a single arbitrary phase offset.

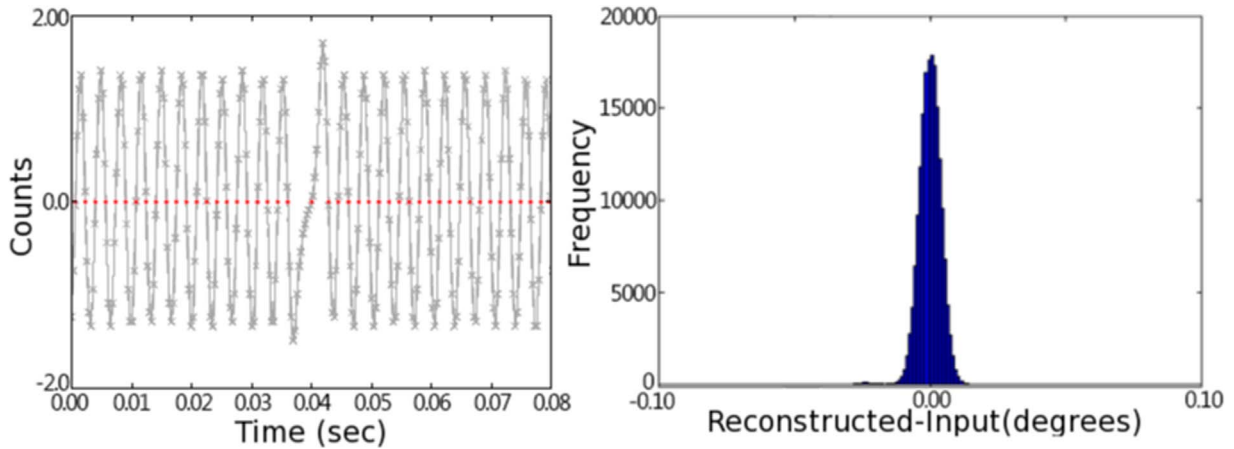
We compared the measured  $\Phi$  to predictions. The phase  $\Phi$  is given by

$$\Phi = -4\theta + 2\beta - 4\mu - 4\delta_{\text{readout}} - 4\Delta_\phi(\nu), \quad (7)$$

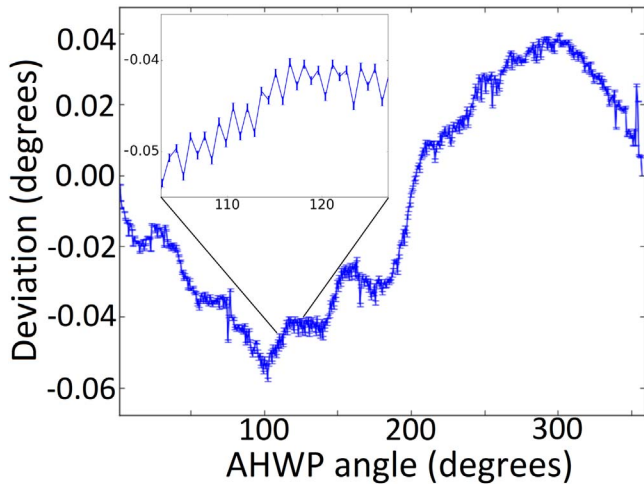
where  $\theta$  is the angle between the angle-encoding LED and the  $+Q$  orientation,  $\beta$  is the angle between the transmission axis of the polarizing grid and  $+Q$ , and  $\mu$  is the angle between the ordinary axis of the AHWP and the double slot; see Figure 29. Time delays between the readout of the HWP angle and the detector data give rise to an offset angle encoded by  $\delta_{\text{readout}}$ . The achromatic nature of the HWP gives a frequency-dependent offset  $\Delta_\phi(\nu)$  (see Section 4.1). Following the right-hand rule, a positive angle corresponds to a counter-clockwise rotation when viewing the focal plane from above.

We used a coordinate measuring machine to determine the axes defining the angles  $\theta$ ,  $\beta$ , and  $\mu$ . Through an analysis of the firmware we determined that  $\delta_{\text{readout}}$  was 10.69 ms. This delay corresponded to a  $7^\circ.6$  rotation of the AHWP at the 1.98 Hz rotation frequency of the AHWP used during both calibrations. The orientation of the effective ordinary axis of the AHWP is frequency dependent. The effective ordinary

<sup>42</sup> Emerson and Cuming, Inc.



**Figure 25.** Left: raw time domain angle-encoding signal over one period of rotation after subtraction of an offset and a gradient. The wider pulse in the middle is the arbitrary zero-angle mark. Red marks denote zero-level crossings. The temporal separation of the marks is assigned a fixed  $0^\circ 75$  angle separation. Right: histogram of the difference between the input angle and reconstructed angle in a simulation of the HWP angle reconstruction pipeline. The standard deviation is  $0^\circ 01$ .



**Figure 26.** Angle reconstruction over 4176 rotations, folded rotation by rotation and averaged. A linear increase between  $0^\circ$  and  $360^\circ$  has been removed. The deviations from zero are due to speed variations. The inset shows the effects of a nonuniform duty cycle in the chopper encoding the angle; see text.

axis over a band up to  $\sim 600$  GHz was determined and marked on the AHWP using the Fourier transform spectroscopy transmission measurements described in Section 4.1. We used measured values for the index of refraction of sapphire at cryogenic temperatures (Loewenstein et al. 1973; Afsar & Chi 1991) to model the expected frequency dependence of the AHWP at its operating temperature and derived values for  $\Delta_\phi(\nu)$  for each of the calibration tests. They are given in Table 6.

The results for the prediction of  $\Phi$  are shown in Figure 28 (blue dashed line). We find an offset of  $12^\circ$  between the prediction and the measurements, and we ascribe this difference to an offset of  $3^\circ$  in the determination of the axis defining  $\mu = 0$ . This is the ordinary axis of the HWP as determined during spectroscopy in the zero-path difference position. The adjusted prediction is shown in the figure as a blue band. There is an uncertainty in the determination of each of the terms in Equation (7). This uncertainty leads to an uncertainty in the predicted  $\Phi$ , which gives the width of the blue band. The sources of uncertainty are tabulated in Table 7.

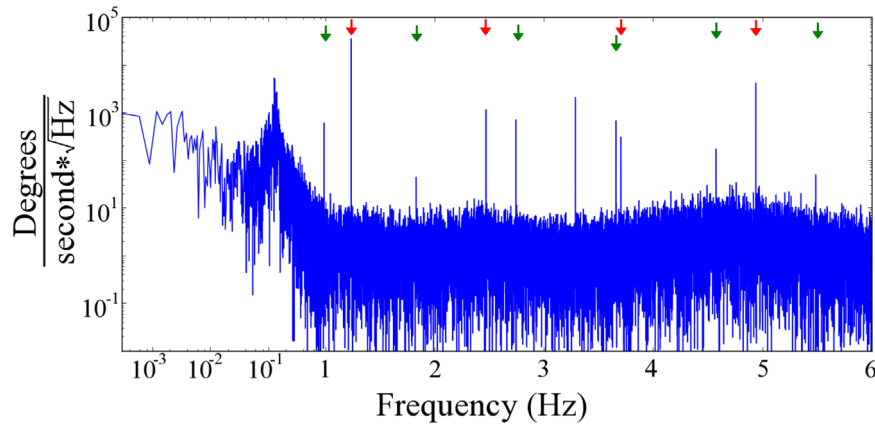
#### 4.4.2. Polarization Modulation Efficiency

The PME of a polarimeter is the ratio of the measured to input level of polarization. We deduce the predicted PME of the AHWP from Fourier transform spectroscopy transmission measurements as described in Section 4.1. The predicted PME for the three frequency bands is given in Table 8. We measured the PME using the Ebert–Fastie spectrometer, described in Section 2.6. We replaced the diffraction grating with a flat aluminum panel to enable broadband measurements with the blackbody source. We placed a polarizing grid at the output of the Ebert–Fastie spectrometer so that the light entering the receiver was to a good approximation fully linearly polarized. The polarized light was temporally chopped by the chopper at the output of the spectrometer and coupled to one detector at a time. We measured the PME by monitoring the detector response to chopped light as a function of orientation of the Ebert–Fastie polarizer. An example measurement of a 250 GHz detector is shown in Figure 30. The average PME measured for each of the three frequency bands is given in Table 8. To our knowledge the EBEX AHWP fractional bandwidth of 109% is the broadest band response of any HWP reported to date.

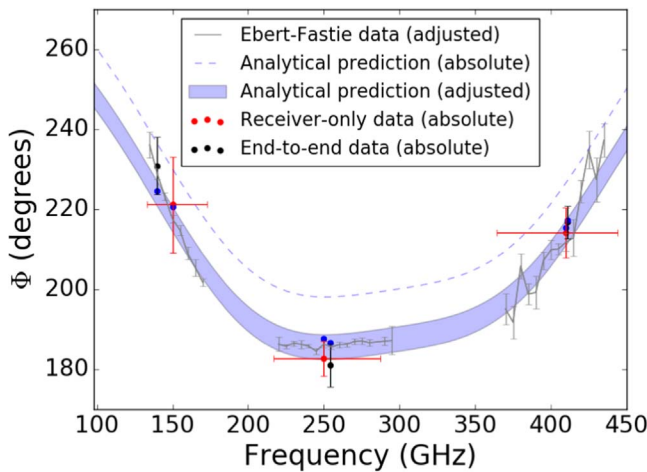
## 5. Summary

EBEX was the first balloon-borne experiment to probe the CMB polarization with a kilopixel array of TES bolometric detectors. The optical system consisted of two ambient temperature aluminum mirrors and four cryogenically cooled PE lenses to increase the throughput and to form a flat and telecentric focal surface for each of the two focal planes. The total throughput per focal plane was  $115 \text{ cm}^2 \text{ sr}$ .

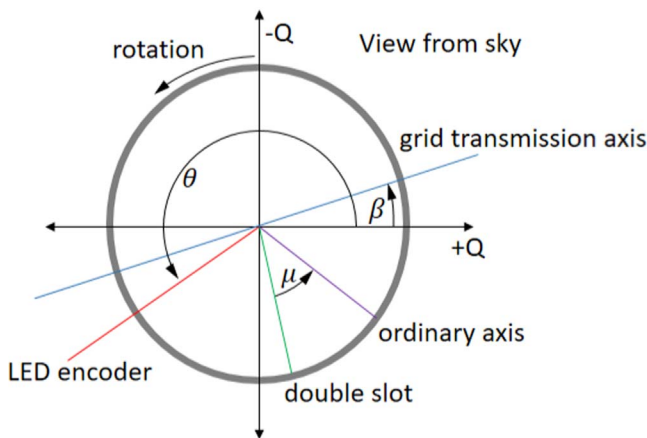
We used a stack of five sapphire half-wave plates to form an AHWP that had a fractional bandwidth of 109%. To our knowledge, this is the broadest fractional bandwidth with which an AHWP has been used to date. The AHWP was levitated by means of an SMB, the first such application in astrophysics. It was rotated continuously at a rate of 1.235 Hz with power dissipation of 15 mW on the 4 K stage. Six mechanical bearings that were implemented as part of the drive train executed more than 1.5 million rotations over 10 days. Rotational speed stability was 0.45% over a period of 10 hr when averaging angular decoding over  $1^\circ 5$ . We reconstructed the angle with an uncertainty of  $0^\circ 01$ , a factor of more than 10 smaller than required for measurements of



**Figure 27.** Power spectrum of 60 minutes of SMB rotation speed data. The horizontal axis is logarithmic at frequencies below 1 Hz and linear above. High- $Q$  peaks are present at the rotation speed and its harmonics (red arrows) and at 0.91 Hz and its harmonics (green arrows).



**Figure 28.** Results of the two polarization rotation calibration tests (black and red data points) and the predicted phase  $\Phi$  as a function of frequency (blue dashed line and band; see text). We also measured the relative phase within each band using an Ebert–Fastie spectrometer (gray); all the data points for a given band were adjusted with a single arbitrary phase offset to fit the predicted phase.



**Figure 29.** Angles that determine the calibration of polarization rotation.

the tensor-to-scalar ratio of  $r = 0.05$ . We calibrated the polarimetric response using double temporal modulation to eliminate sources of systematic uncertainty.

EBEX had three frequency bands centered on 150, 250, and 410 GHz, all sharing the same refractive/reflective optical

**Table 7**  
Uncertainties for Each of the Parameters in the Prediction of  $\Phi$

Parameter	Uncertainty	Source
$\theta$	$<0^\circ.1$	Geometrical measurement error
$\beta$	$<0^\circ.1$	Geometrical measurement error
	$0^\circ.25$	Uncertainty in transmission axis measurement
$\mu$	$<0^\circ.1$	Geometrical measurement error
$\Delta_\phi$	$0^\circ.7$	Uncertainty in AHWP model
$\delta_{\text{readout}}$	$<0^\circ.1$	AHWP speed variations
Total	$0^\circ.8$	

**Note.** The total is a quadrature addition of the individual contributions.

**Table 8**  
Predicted and Measured PME for Each Frequency Band

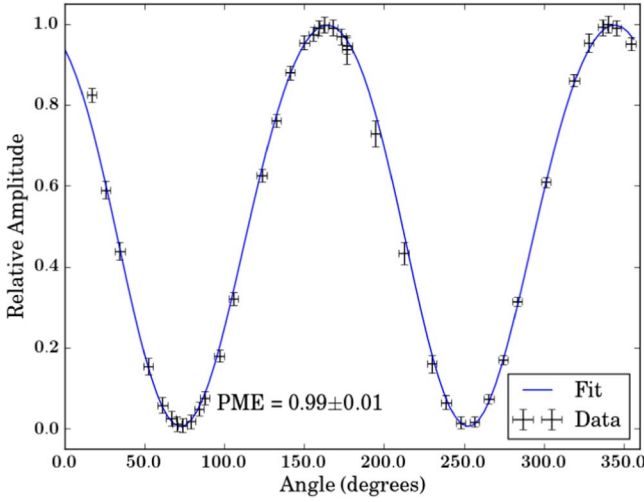
Frequency Band	Prediction	Measured
150 GHz	0.99	$0.98 \pm 0.06$
250 GHz	1.0	$0.98 \pm 0.02$
410 GHz	0.92	$0.92 \pm 0.06$

**Note.** The predictions were calculated using the Fourier transform spectroscopy measurements described in Section 4.1 and assume a flat input spectrum. The measured values are a weighted average over seven, four, and nine detectors at 150, 250, and 410 GHz, respectively.

train. We used broadband ARC that consisted of glued layers of porous Teflon on the lenses and a combination of TMM and Teflon on the AHWP. Polyethylene and Stycast were used as glues. As a consequence, the system has an approximately achromatic response with 60%–70% transmission over the entire range of frequencies. For an optical system using refractors, this is the broadest fractional bandwidth operated simultaneously by any CMB experiment to date.

The receiver that was built to house the cold optics performed according to specifications, giving focal plane temperatures near 250 mK and temperature stability with  $1/f$  knee at 2 mHz. We implemented a double vacuum window mechanism to reduce emission from a thick vacuum window at float altitudes.

With EBEX we were the first to implement on a balloon platform many of the technologies characterizing present-day high-throughput CMB polarimetric instruments. These use high-throughput optical systems and arrays with thousands of



**Figure 30.** Measurement of the PME with one 250 GHz detector. Data points are the detector response at the frequency of the temporally modulated input radiation as a function of the rotation angle of the grid defining the input polarization.

transition edge bolometric sensors that are massively multiplexed. For polarimetry we used a continuously rotating AHWP, one of an array of techniques being explored by the CMB community in the search for the inflationary signal.

Two companion papers provide additional details about the EBEX detectors, their readout, and their flight performance (EP2) and about the gondola, the attitude control system, and other support systems (EP3).

Support for the development and flight of the EBEX instrument was provided by NASA grants NNX12AD50G, NNX13AE49G, NNX08AG40G, and NNG05GE62G and by NSF grants AST-0705134 and ANT-0944513. We acknowledge support from the Italian INFN INDARK Initiative. P.A. and C.T. acknowledge the Science & Technology Facilities Council for its continued support of the underpinning technology for filter and wave plate development. We also acknowledge support by the Canada Space Agency, the Canada Research Chairs Program, the Natural Sciences and Engineering Research Council of Canada, the Canadian Institute for Advanced Research, the Minnesota Supercomputing Institute, the National Energy Research Scientific Computing Center, the Minnesota and Rhode Island Space Grant Consortia, our collaborating institutions, and Sigma Xi, The Scientific Research Society. Baccigalupi acknowledges support from the RADIOFOREGROUNDS grant of the European Union’s Horizon 2020 research and innovation program (COMPET-05-2015, grant agreement no. 687312) and the INDARK INFN Initiative. J.D. acknowledges a NASA NESSF fellowship NNX11AL15H. B.R.-K. acknowledges an NSF Post-Doctoral Fellowship AST-1102774 and a NASA Graduate Student Research Fellowship. K.R. and K.Z. acknowledge support by the Minnesota Space Grant Consortium. We very much thank Danny Ball and his colleagues at the Columbia Scientific Balloon Facility for their dedicated support of the EBEX program. We are grateful for contributions to the fabrication of optical elements by Enzo Pascale and Lorenzo Monceli. Xin Zhi Tan’s and Chiou Yang Tan’s help with figures is acknowledged and much appreciated.

## Appendix A

### Double Modulation/Demodulation and Extracting $\Phi$

We consider the signal recorded due to a source that is chopped between two intensities, polarized at angle  $\alpha_{\text{in}}$ , and detected by a polarimeter with an HWP and a polarizing grid. We are only interested in linearly polarized light; therefore, the input Stokes vector is

$$S_{\text{in}} = \begin{bmatrix} I \\ Q \\ U \end{bmatrix}, \quad (8)$$

with

$$X = \sum_l X_l \cos(l\omega_c t + \phi_{c,l}), \quad X = I, Q, U, \quad (9)$$

where  $\omega_c$  is the chopping frequency. We include an arbitrary number of  $l$  harmonics in  $X$  because the chopping is not necessarily sinusoidal. Typically the  $l = 0, 1$  components dominate, giving

$$X_{01} = X_0 + X_1 \cos(\omega_c t + \phi_c), \quad X = I, Q, U. \quad (10)$$

The rotation of the HWP modifies  $S_{\text{in}}$  to give

$$S_{\text{in}} = \begin{bmatrix} I \\ \epsilon [Q \cos(4\gamma) + U \sin(4\gamma)] \\ \epsilon [Q \sin(4\gamma) - U \cos(4\gamma)] \end{bmatrix}, \quad (11)$$

where  $\gamma = \omega_{\text{hwp}} t$  is the rotation angle. After the analyzer grid, which is oriented at an angle  $\beta$ , we have the TOD

$$D(t) = \frac{1}{2} \{I + \epsilon [Q \cos(4\gamma - 2\beta) + U \sin(4\gamma - 2\beta)]\}. \quad (12)$$

In the ideal case the HWP is rotating at a constant rate  $\dot{\gamma} = \omega_{\text{hwp}}$ . In practice, and as we showed in Figure 27, the rotation rate is not constant. The constant term is dominant, but there are also subdominant terms at frequencies that are harmonics of the rotation rate. Thus, the angle  $\gamma(t)$  should more generally be written as

$$\gamma(t) = \omega_{\text{hwp}} t + \sum_m b_m \cos(m\omega_{\text{hwp}} t). \quad (13)$$

We first highlight the most dominant properties of the TOD by assuming a purely sinusoidal chop and constant rotation rate, that is, using Equation (10) and  $\dot{\gamma} = \omega_{\text{hwp}}$ . We also include the phase  $\Phi$  and spurious polarization signals that are not chopped (see Section 4.4),

$$\begin{aligned} D(t) = & \frac{1}{2} (I_0 + I_1 \cos(\omega_c t + \phi_c)) \\ & + \frac{\epsilon}{2} \{Q_0 \cos(4\gamma - \Phi) + Q_1 [\cos(4\omega_{\text{hwp}} t - \Phi) \cos(\omega_c t + \phi_c)] \\ & + U_0 \sin(4\gamma - \Phi) + U_1 [\sin(4\omega_{\text{hwp}} t - \Phi) \cos(\omega_c t + \phi_c)]\} \\ & + \sum_j A_j \cos(j\omega_{\text{hwp}} t + \phi_j). \end{aligned} \quad (14)$$

The  $Q_0, U_0$  signals are at a frequency of  $4\omega_{\text{hwp}}$ , but so is the spurious signal term  $A_4$ . The components  $Q_1, U_1$  are at frequencies  $4\omega_{\text{hwp}} \pm \omega_c$ , which are sidebands of  $4\omega_{\text{hwp}}$ . Since

$Q_1$ ,  $U_1$  are known—specifically, the incident polarization angle is given by  $\alpha_{\text{in}} = (1/2)\arctan(U_1/Q_1)$ —analysis of the signal at these sidebands gives  $\Phi$  without contamination by the spurious signal terms.

The product of the harmonic series in  $X$  (Equation (9)) and the multiplicity of frequencies in  $\gamma$  (Equation (13)) generate additional sidebands, some of which overlap with  $4\omega_{\text{hwp}} \pm \omega_c$ . Bandpassing the raw TOD around these sidebands before the double demodulation rejects other sidebands. We estimated the contributions of terms that do not include  $Q_1$ ,  $U_1$  to the sidebands  $4\omega_{\text{hwp}} \pm \omega_c$  and concluded that they would change the determination of  $\Phi$  by 0.2 at most. We therefore proceeded with the analysis using Equation (14).

Double demodulation consists of multiplying the bandpassed version of  $D(t)$  by a reference chopper signal and a reference HWP signal. One can bandpass around and use both sidebands or bandpass around and use just one of the sidebands. Using both sidebands gains a factor of 2 in signal relative to a single sideband; doing the analysis separately on each sideband can be used as an internal cross-check, or to determine the bolometer time constant, as discussed in Appendix B. Below we assume an analysis that uses both sidebands. We derive the reference chopper signal by bandpassing  $D(t)$  with a 0.7 Hz filter centered on  $\omega_c$ . We derive the reference HWP signal using the angular encoding information of the HWP.

After bandpassing the TOD is

$$\begin{aligned} D'(t) = & \frac{\epsilon}{4} \{ Q_1 [\cos(4\omega_{\text{hwp}}t - \Phi + \omega_c t + \phi) \\ & + \cos(4\omega_{\text{hwp}}t - \Phi - \omega_c t - \phi)] \\ & + \frac{\epsilon}{4} \{ U_1 [\sin(4\omega_{\text{hwp}}t - \Phi + \omega_c t + \phi) \\ & + \sin(4\omega_{\text{hwp}}t - \Phi - \omega_c t - \phi)] \}. \end{aligned} \quad (15)$$

Multiplying by the chopper reference signal gives

$$\begin{aligned} D''(t) = & D'(t)\cos(\omega_c t + \phi) \\ = & \frac{\epsilon}{4} Q_1 \{ \cos(4\omega_{\text{hwp}}t - \Phi) \\ & + \frac{1}{2} [\cos(4\omega_{\text{hwp}}t - \Phi - 2\omega_c t - 2\phi) \\ & + \cos(4\omega_{\text{hwp}}t - \Phi + 2\omega_c t + 2\phi)] \} \\ & + \frac{\epsilon}{4} U_1 \{ \sin(4\omega_{\text{hwp}}t - \Phi) \\ & + \frac{1}{2} [\sin(4\omega_{\text{hwp}}t - \Phi - 2\omega_c t - 2\phi) \\ & + \sin(4\omega_{\text{hwp}}t - \Phi + 2\omega_c t + 2\phi)] \}. \end{aligned} \quad (17)$$

Multiplying by the two HWP reference signals  $\cos 4\gamma$  and  $\sin 4\gamma$  and low-passing at 0.7 Hz gives

$$D''(t)\cos 4\gamma_{\text{DC}} = \frac{\epsilon}{8} [Q_1 \cos(\Phi) - U_1 \sin(\Phi)] \quad (18)$$

$$D''(t)\sin 4\gamma_{\text{DC}} = \frac{\epsilon}{8} [Q_1 \sin(\Phi) + U_1 \cos(\Phi)], \quad (19)$$

where the subscript  $\text{DC}$  indicates that we are keeping only the zero-frequency term; the low-pass filter suppresses the other terms. Because  $\alpha_{\text{in}} = (1/2)\arctan(U_1/Q_1)$ , we can rewrite

$D''(t)$  as

$$\begin{aligned} D''(t)\cos 4\gamma_{\text{DC}} = & \frac{\epsilon}{8} \left( \frac{Q_1}{\cos(2\alpha_{\text{in}})} \right) [\cos(2\alpha_{\text{in}})\cos(\Phi) \\ & - \sin(2\alpha_{\text{in}})\sin(\Phi)] \\ = & \frac{\epsilon}{8} \left( \frac{Q_1}{\cos(2\alpha_{\text{in}})} \right) \cos(2\alpha_{\text{in}} + \Phi) \end{aligned} \quad (20)$$

$$\begin{aligned} D''(t)\sin 4\gamma_{\text{DC}} = & \frac{\epsilon}{8} \left( \frac{Q_1}{\cos(2\alpha_{\text{in}})} \right) [\cos(2\alpha_{\text{in}})\sin(\Phi) \\ & + \sin(2\alpha_{\text{in}})\cos(\Phi)] \\ = & \frac{\epsilon}{8} \left( \frac{Q_1}{\cos(2\alpha_{\text{in}})} \right) \sin(2\alpha_{\text{in}} + \Phi), \end{aligned} \quad (21)$$

and solve for  $\Phi$ ,

$$\Phi = \arctan \left( \frac{[D''(t)\sin(4\gamma)]_{\text{DC}}}{[D''(t)\cos(4\gamma)]_{\text{DC}}} \right) - 2\alpha_{\text{in}}. \quad (22)$$

## Appendix B Estimates of Bolometer Time Constants

### B.1. Single-pole Response

We assumed that the bolometer time constant follows a single-pole response with critical frequency  $\omega_b = 2\pi f_b = 1/\tau_b$  and used the polarization calibration data to estimate it. A single-pole response gives rise to attenuation of signals at frequencies near and above  $\omega_b$  and to a frequency-dependent phase shift. We investigated the use of both effects to estimate the time constant.

As described in Section 4.4.1 and in Appendix A, the polarization calibration relies on signals that are in frequencies  $4\omega_{\text{hwp}} + \omega_c$  and  $4\omega_{\text{hwp}} - \omega_c$ . The “attenuation” method relies on the observation that for the relevant range of  $\omega_b$ ,  $\omega_{\text{hwp}}$ , and  $\omega_c$  there is more attenuation of power in the higher sideband than in the lower. We used the ratio of powers in the two sidebands to estimate  $\tau_b$ . The “phase” method relies on the fact that the signal at the higher-frequency sideband undergoes a larger phase shift compared to the signal at the lower frequency. Thus, an analysis extracting the calibration angle  $\Phi$  from each of these signals *without* first deconvolving the bolometer temporal response gives a difference in angle  $\Phi$  with a magnitude that depends on  $\tau_b$ . We used the phase method because simulations showed that the attenuation method was prone to larger bias at high noise levels. Here we describe the phase method; Klein (2014) gives more details on both approaches.

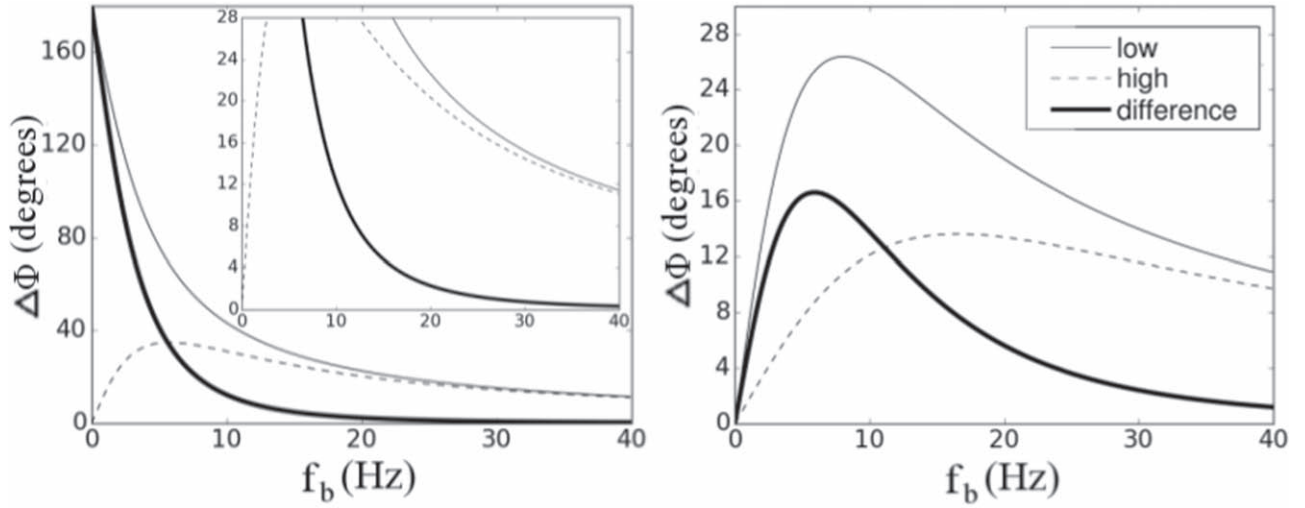
Relative to an infinitely fast detector, each frequency component of the signal undergoes a phase shift

$$\delta(\omega) = -\arctan(\omega\tau_b). \quad (23)$$

Analyzing the raw data for  $\Phi$  as described in Appendix A, that is, without deconvolving a bolometer response function, and using each sideband separately, we find

$$\Phi_{\text{obs,low}} = \Phi_0 - \frac{1}{2}(\delta_{\text{low}} + \delta_c) \quad (24)$$





**Figure 31.** Values of  $\Delta\Phi_{\text{obs}}$  as a function of  $f_b$  for  $f_{\text{hwp}} = 2$  Hz and  $f_c = 3$  Hz that were used for the receiver-only polarization calibration (left) and for  $f_{\text{hwp}} = 2$  Hz and  $f_c = 13$  Hz that were used for the entire-instrument polarization calibration (right). The panels also show the phases  $\delta_{\text{low}}$  and  $\delta_{\text{high}}$  (light gray). For  $f_c < 4f_{\text{hwp}}$  we show  $\Delta\Phi_{\text{obs}}$  over all possible phase differences and in the inset over the range that matches the panel for  $f_c > 4f_{\text{hwp}}$ .

and

$$\Phi_{\text{obs,high}} = \Phi_0 - \delta_{\text{high}} - \delta_c, \quad (25)$$

where  $\Phi_{\text{obs,low}}$  and  $\Phi_{\text{obs,high}}$  are the extracted  $\Phi$  values from the low and high sidebands, respectively.  $\Phi_0$  is the nominal value, i.e., the value we would extract with an infinitely fast time constant (or with a perfect deconvolution). The quantities  $\delta_{\text{low}}$ ,  $\delta_{\text{high}}$ , and  $\delta_c$  are the phase shifts due to the bolometer time constant at the low and high sidebands and the chop frequency, respectively. The phase difference  $\Delta\Phi_{\text{obs}} \equiv \Phi_{\text{obs,low}} - \Phi_{\text{obs,high}}$  is given by

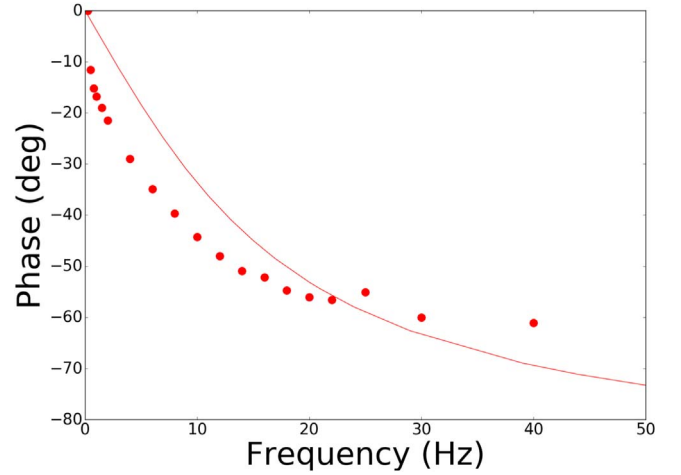
$$\begin{aligned} \Delta\Phi_{\text{obs}} &= \delta_{\text{high}} - \delta_{\text{low}} - 2\delta_c \\ &= \arctan((4\omega_{\text{hwp}} - \omega_c)\tau) - \arctan((4\omega_{\text{hwp}} + \omega_c)\tau) \\ &\quad + 2\arctan(\omega_c\tau). \end{aligned} \quad (26)$$

Figure 31 shows  $\Delta\Phi_{\text{obs}}$  as a function of  $\omega_b$ . When  $\omega_c < 4\omega_{\text{hwp}}$  a value of  $\Delta\Phi_{\text{obs}}$  uniquely determines  $\omega_b$ . When  $\omega_c > 4\omega_{\text{hwp}}$ , a value of  $\Delta\Phi_{\text{obs}}$  gives two possible values of  $\omega_b$ .

In the receiver-only polarization calibration  $f_c$  and  $4f_{\text{hwp}}$  were 3 and 8 Hz, respectively. In the entire-instrument calibration  $f_c$  and  $4f_{\text{hwp}}$  were 13 and 8 Hz, respectively. For this test we used the attenuation method in combination with the phase method to break the degeneracy between the two possible values of  $f_b$ . Typical values for  $f_b$  were close to 5 Hz.

### B.2. Deviations from Single-pole Response

We measured the frequency response due to the bolometer time constant by correlating the chopper signal as recorded by the detectors and the input chopper signal for chopper frequencies between near 0 and 40 Hz. The difference in phase gave the frequency response of the bolometer. For the 350 bolometers measured, we found that the bolometer time constant deviated from a single-pole response. An example is shown in Figure 32. The deviation entails a necessary correction to the extraction of the phase  $\Phi$ . Because we did not measure the individual frequency response of all the bolometers, we applied an overall correction based on the



**Figure 32.** Relative phase between an input and measured chopper signal as a function of the frequency of the chopper (dots) for one detector. The relative phase is due to the bolometer time constant, which does not follow a pure single-pole model (solid line).

**Table 9**  
Polarization Rotation Correction due to the Assumption of Single-pole Response


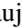




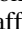
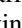
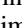


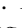

Frequency Band	Receiver-only Test	End-to-end Calibration
150 GHz	4°1	0°0
250 GHz	1°5	3°5
410 GHz	1°9	2°1

ensemble of frequency responses measured. We now describe this correction.

We generated simulated TOD for each of the 350 measured frequency responses with a known input  $\Phi$ . The simulated data were subject to the polarization calibration data analysis, still under the assumption that the detectors were modeled by a single-pole filter. The difference between the input and the mean extracted  $\Phi$  quantified the bias introduced by the assumption of a single-pole response. Table 9 gives the phase

shifts  $\Phi$  measured for each of the two polarization rotation calibrations and for each frequency band.

### ORCID iDs

Peter Ade  <https://orcid.org/0000-0002-5127-0401>  
 Derek Araujo  <https://orcid.org/0000-0003-0527-2948>  
 François Aubin  <https://orcid.org/0000-0002-8241-4156>  
 Joy Didier  <https://orcid.org/0000-0003-4151-9450>  
 Shaul Hanany  <https://orcid.org/0000-0002-8702-6291>  
 Kyle Helson  <https://orcid.org/0000-0001-9238-4918>  
 Andrew Jaffe  <https://orcid.org/0000-0003-2086-1759>  
 Lorne Levinson  <https://orcid.org/0000-0003-4679-0485>  
 Michele Limon  <https://orcid.org/0000-0002-5900-2698>  
 Ilan Sagiv  <https://orcid.org/0000-0001-8377-3153>  
 Gregory S. Tucker  <https://orcid.org/0000-0002-6954-6947>  
 Karl Young  <https://orcid.org/0000-0002-1337-6088>  
 Kyle Zilic  <https://orcid.org/0000-0003-1971-7151>

### References

- Ade, P., Akiba, Y., Anthony, A., et al. 2014, *ApJ*, **794**, 171  
 Ade, P. A. R., Pisano, G., Tucker, C., & Weaver, S. 2006, *Proc. SPIE*, **6275**, 0U  
 Afsar, M. N., & Chi, H. 1991, *Proc. SPIE*, 1576, 0U  
 Aubin, F. 2012, PhD thesis, McGill Univ.  
 Aubin, F., Aboobaker, A. M., Ade, P., et al. 2010, *Proc. SPIE*, **7741**, 1T  
 Aubin, F., Aboobaker, A. M., Ade, P., et al. 2016, arXiv:1601.07923  
 Baumann, D., Jackson, M. G., Adshead, P., et al. 2009, *AIPC*, **1141**, 10  
 Benoît, A., Ade, P., Amblard, A., et al. 2002, *Aph*, **17**, 101  
 BICEP2 Collaboration, Ade, P. A. R., Aikin, R. W., et al. 2014, *PhRvL*, **112**, 241101  
 BICEP2/Keck and Planck Collaborations, Ade, P. A. R., Aghanim, N., et al. 2015, *PhRvL*, **114**, 101301  
 Bock, J. J., Parikh, M. K., Fischer, M. L., & Lange, A. E. 1995, *ApOpt*, **34**, 4812  
 Chapman, D. 2015, PhD thesis, Columbia Univ.  
 Chapman, D., Aboobaker, A., Araujo, D., et al. 2015, in IEEE Aerospace Conf.  
 Didier, J. 2016, PhD thesis, Columbia Univ.  
 Didier, J., Chapman, D., Aboobaker, A., et al. 2015, in IEEE Aerospace Conf., 7119010  
 Dragone, C. 1982, *ITAP*, **30**, 331  
 Fastie, W. G. 1952a, *JOSA*, **42**, 641  
 Fastie, W. G. 1952b, *JOSA*, **42**, 647  
 Grainger, W., Aboobaker, A. M., Ade, P., et al. 2008, *Proc. SPIE*, **7020**, 2N  
 Hanany, S., Matsumura, T., Johnson, B., et al. 2003, *ITAS*, **13**, 2128  
 Hanson, D., Hoover, S., Crites, A., et al. 2013, *PhRvL*, **111**, 141301  
 Huber, M. E., Neil, P. A., Benson, R. G., et al. 2001, *ITAS*, **11**, 4048  
 Hull, J. R., Mulcahp, T. M., Uherka, K. L., Erck, R. A., & Abboud, R. G. 1994, *ApSup*, **2**, 449  
 King, A. J. 1950, *PIRE*, **38**, 249  
 Klein, J. 2014, PhD thesis, Univ. Minnesota  
 Klein, J., Aboobaker, A., Ade, P., et al. 2011, *Proc. SPIE*, **8150**, 04  
 Kovac, J. M., Leitch, E. M., Pryke, C., et al. 2002, *Natur*, **420**, 772  
 Loewenstein, E. V., Smith, D. R., & Morgan, R. L. 1973, *ApOpt*, **12**, 398  
 MacDermid, K. 2014, PhD thesis, McGill Univ.  
 MacDermid, K., Aboobaker, A. M., Ade, P., et al. 2014, *Proc. SPIE*, **9153**, 915311  
 Matsumura, T. 2006, PhD thesis, Univ. Minnesota  
 Matsumura, T., Hanany, S., Ade, P., et al. 2009, *ApOpt*, **48**, 3614  
 Milligan, M., Ade, P., Aubin, F., et al. 2010, *Proc. SPIE*, **7740**, 07  
 Mizuguchi, Y., Akagawa, M., & Yokoi, H. 1978, *JELCo*, **61**, 58  
 Moncelsi, L., Ade, P. A. R., Angilè, F. E., et al. 2014, *MNRAS*, **437**, 2772  
 Naess, S., Hasselfield, M., McMahan, J., et al. 2014, *JCAP*, **2014**, 007  
 Oxley, P., Ade, P. A., Baccigalupi, C., et al. 2004, *Proc. SPIE*, **5543**, 320  
 Pancharatnam, S. 1955, *InASP*, **41**, 137  
 Planck Collaboration et al. 2016, *A&A*, **594**, A10  
 Polsgrove, D. E. 2009, PhD thesis, Univ. Minnesota  
 Raach, K. 2017, PhD thesis, Univ. Minnesota  
 Reichborn-Kjennerud, B. 2010, PhD thesis, Columbia Univ.  
 Reichborn-Kjennerud, B., Aboobaker, A. M., Ade, P., et al. 2010, *Proc. SPIE*, **7741**, 1C  
 Sagiv, I., Aboobaker, A. M., Bao, C., et al. 2012, in 12th Marcel Grossmann Meeting, ed. A. H. Chamseddine (Singapore: World Scientific Publishing Co.), **2166**  
 Sagiv, I. S. 2011, PhD thesis, Univ. Minnesota  
 Savini, G., Ade, P. A. R., House, J., et al. 2009, *ApOpt*, **48**, 2006  
 Savini, G., Pisano, G., & Ade, P. A. R. 2006, *ApOpt*, **45**, 8907  
 Scott, D., & Smoot, G. F. 2010, arXiv:1005.0555  
 The EBEX Collaboration, Abitbol, M., Aboobaker, A. M., et al. 2018a, *ApJS*, **239**, 8  
 The EBEX Collaboration, Aboobaker, A., Ade, P., et al. 2018b, *ApJS*, **239**, 9  
 Thébault, E., Finlay, C. C., Beggan, C. D., et al. 2015, *EP&S*, **67**, 79  
 Westbrook, B., Lee, A., Meng, X., et al. 2012, *JLTP*, **167**, 885  
 Westbrook, B. G. 2014, PhD thesis, Univ. California, Berkeley  
 Zaldarriaga, M., & Seljak, U. 1997, *PhRvD*, **55**, 1830  
 Zilic, K. 2014, PhD thesis, Univ. Minnesota  
 Zilic, K., Aboobaker, A., Aubin, F., et al. 2017, *RSci*, **88**, 045112